12-1-2020

Observation and simulation of a bifurcating thunderstorm over Beijing

Jingjing Dou
Nanjing University

Robert Bornstein
San Jose State University, robert.bornstein@sjsu.edu

Shiguang Miao
China Meteorological Administration

Jianning Sun
Nanjing University

And Yizhou Zhang
China Meteorological Administration

Recommended Citation

Jingjing Dou, Robert Bornstein, Shiguang Miao, Jianning Sun, and And Yizhou Zhang. "Observation and simulation of a bifurcating thunderstorm over Beijing" *Journal of Applied Meteorology and Climatology* (2020): 2129-2148. https://doi.org/10.1175/JAMC-D-20-0056.1

Observation and Simulation of a Bifurcating Thunderstorm over Beijing

JINGJING DOU,[a,b] ROBERT BORNSTEIN,[b,c] SHIGUANG MIAO,[b] JIANNING SUN,[a] AND YIZHOU ZHANG[b]

[a] *School of Atmospheric Sciences and Institute for Climate and Global Change Research, Nanjing University, Nanjing, China*
[b] *Institute of Urban Meteorology, China Meteorological Administration, Beijing, China*
[c] *Department of Meteorology and Climatology, San Jose State University, San Jose, California*

(Manuscript received 9 March 2020, in final form 8 October 2020)

ABSTRACT: The aim of this study was the analysis and simulation of the life cycle of a bifurcating thunderstorm that passed over Beijing, China, on 22 July 2015. Data from 150 surface weather sites and an S-band radar were used in conjunction with WRF simulations that used its multilevel Building Environment Parameterization (BEP) urbanization option. The Urban-case simulation used Beijing land-use information, and the NoUrban one replaced all urban areas by croplands. The Urban case correctly simulated both the observed weak 10-m winds over Beijing ($<1.0\,m\,s^{-1}$) and the weak 2-m urban heat island ($<0.5°C$). Observed radar and rain gauge data, as well as the Urban-case results, all showed precipitation bifurcation around Beijing, with maximum accumulations in convergent flow areas on either side of the city. The Urban case also reproduced the observed precipitation minima over the urban area and in a downwind rain shadow. The observations and Urban-case results both also showed bifurcated flow, even when the storm was still upwind of Beijing. The subsequent bifurcated precipitation areas thus each moved along a preexisting flow branch. Urban-case vertical sections showed downward motion in the divergence areas over the urban core and upward motions over the lateral convergence zones, both up to 6 km. Given that the NoUrban case showed none of these features, these differences demonstrate how the impact of cities can extend upward into deep local convection. Additional case-study simulations are needed to more fully understand urban storm bifurcation mechanisms in this and other storms for cities in a variety of climates.

KEYWORDS: Rainfall; Anthropogenic effects; Numerical analysis/modeling; Urban meteorology

1. Introduction

Many investigations of the complex ways in which urban areas impact weather and climate have been carried out, and thus urban areas are known to modify temperatures, humidity, wind, and precipitation (Dou and Miao 2017; Oke et al. 2017; Zhang et al. 2019; An et al. 2020). Uncertainties, however, remain about urban impacts on precipitation (Shepherd 2013; Han et al. 2014; Mitra and Shepherd 2016). Urban effects on precipitation were the focus of the classic 1970s Metropolitan Meteorological Experiment (METROMEX) climatological field study, which investigated summer convective rainfall over Saint Louis, Missouri. Observations showed precipitation increases within the city and at 50–75 km downwind, as summarized by Changnon et al. (1991). Similar results for other cities were also seen by Shepherd et al. (2002) and Schlünzen et al. (2010).

Radar observations by Haberlie et al. (2015), however, showed only the existence of urban heat island (UHI) initiated isolated convective events over Atlanta, Georgia. The radar observations of Bornstein and LeRoy (1990) for New York City (NYC), New York, over two summers and by Bornstein and Lin (2000) for five events over Atlanta showed individual storms either initiated by an UHI or bifurcated by the building barrier, that is, a building induced splitting upwind of an urban area, followed by movement around the city, and then downwind merging. Deflecting or bifurcation of storms were also observed in Berlin by Lorenz et al. (2019), while the observations by Niyogi et al. (2011) showed storms that were either initiated, dissipated, intensified, or bifurcated over Indianapolis, Indiana. Regional-scale observations of urban increases on precipitation have also been carried out in China (Luo et al. 2016; Wu et al. 2019; Jiang et al. 2020). Beijing, China, has also shown urban modifications; for example, Wu et al. (2000) and Sun et al. (2006) both showed UHI related increases in short duration precipitation over the city of Beijing and downwind.

To address the "conflicting" impacts (i.e., downwind vs overcity maxima), Bornstein (2011) hypothesized that strong UHIs initiate convective activity (and thus produce a city center precipitation maximum) during periods with near-calm regional flows. During strong wind and weak UHI conditions, however, moving storms bifurcate, producing precipitation minima over and downwind of cities (i.e., an urban rain-shadow effect). It also produces maxima, both in the lateral boundary convergence zones around the city (where the bifurcated flows converge with the undisturbed flows) and in their downwind reconvergence region. He thus identified UHI intensity as the key determinant as to which of the two impacts occurs (while synoptic flow direction determines where it occurs), as it integrates the urban impacts on energy fluxes, wind, and stability. This hypothesis thus identified the specific urban impacts producing each of the above effects: downwind urban edge maxima of METROMEX, city center maxima (Bornstein and Lin 2000), and bifurcation (Niyogi et al. 2011). Bornstein (2011) did not evaluate the UHI magnitude for each of his NYC cases, he just assumed it as the key parameter. He did note, however, that the value would vary from city to city, dependent on city size and morphology.

Dou et al. (2015), however, did a climatological analysis of many Beijing summer storms, which included evaluation of the

Corresponding author: Jingjing Dou, jjdou@ium.cn

DOI: 10.1175/JAMC-D-20-0056.1

UHI magnitude for each. Results showed it (in conjunction with regional flow direction) as the key determinant of which urban effect will predominate. They found an average UHI value of 1.25°C in the summer for Beijing. Storms with UHI values greater than this average induced or strengthened thunderstorm formation, which produced an enhanced maximum of precipitation over central Beijing. Weaker UHIs (than this average), however, produced storms that bifurcated over Beijing, producing minima over both the urban center and in a downwind urban rain shadow. Maxima were also seen along the downwind lateral edges of the urban area.

Modeling allows for controlled experiments to characterize urban processes for weather and climate applications (Chen et al. 2011; Zhang et al. 2019; Zhang 2020). A study with the fifth-generation Pennsylvania State University–National Center for Atmospheric Research Mesoscale Model (MM5) by Craig and Bornstein (2002) showed a storm arising from UHI induced convergence into Atlanta. The rain was centered over the city, while a second simulation without the city produced no storm. Simulations of two storms over Atlanta by Shem and Shepherd (2009) used the Weather Research and Forecast (WRF) Model with its Noah land-use scheme, which represents urban areas by only changes in surface parameters. Results showed UHI initiation in one case and urban enhancement in the other. Li et al. (2013) used WRF linked to its Single Layer Urban Canopy Model (SLUCM; Kusaka et al. 2001) to investigate precipitation patterns during a summer storm over Baltimore, Maryland. Similar case-study simulations of nonbifurcating summer storms over Beijing have been carried out, for example, WRF-SLUCM simulations by Zhong and Yang (2015). Use of the WRF multilevel Building Environment Parameterization (BEP; Martilli et al. 2002) by Yu and Liu (2015) showed that Beijing produced up- and downstream precipitation increases that are due to enhanced urban heat fluxes.

Simulations of bifurcating storms over Beijing have also been carried out; for example, the use of MM5 by Guo et al. (2006) for a weak UHI case showed upwind bifurcation. Simulations by Miao et al. (2011) with WRF-SLUCM showed that early urbanization decreased maximum rainfall over the city due to urban surface dryness. Further urbanization produced additional decreases as storms started to bifurcate around Beijing. Zhang et al. (2017) simulated two Beijing summer storms with the same model pair and showed contrasting urban effects under strong and weak UHI conditions, that is, initiation versus bifurcation, respectively.

Whereas previous modeling case studies have investigated urban impacts on bifurcating summer convective storms, the present study is the first (to our knowledge) to do so with WRF and its multilevel BEP urbanized scheme. The study is thus able to investigate the fine-temporal-scale (15 min) dynamic details of a well-documented, clear signal, bifurcating summer storm over Beijing during weak UHI conditions. Detailed analyses of the observed and simulated urban precipitation patterns are carried out, and some simulated planetary boundary layer (PBL) dynamical processes producing the urban impacts are investigated.

2. Data and model description

The intensive 2014–19 Beijing Study of Urban Impacts on Rainfall and Fog/Haze (SURF) Project was organized by the Institute of Urban Meteorology (IUM). The Institute is in Beijing and is both a China Meteorological Administration (CMA) urban PBL research center and an operational WRF numerical weather prediction (NWP) forecast center (Liang et al. 2018). The study was carried out to better understand and model interactions between urban, topographic, PBL, and convective processes for both summer storm events and winter high concentration aerosol events.

One of the largest metropolitan regions worldwide, the greater Beijing area (GBA) is in the north China plain (Fig. 1a), east of the Taihang Mountains, and south of the more distant Yanshan Mountains (Fig. 1b). Urban Beijing has undergone significant growth (at the expense of its surrounding cropland) during the past several decades (Dou et al. 2014), and its built-up area has increased from 500 to 1300 km^2 during 2000–15 (Wang et al. 2010) while its population increased from 14 to 22 million (Beijing Municipal Bureau of Statistics 2016). Its transportation system includes six concentric automobile ring roads (RRs), with the areas within each having different population and building densities (Jacobson et al. 2015). The densest/tallest buildings and most populated areas are mainly within RR 4 (Kuang and Du 2011), located 8 km from the city center and with approximate circumference of about 65 km.

a. Data description

A 22 July 2015 thunderstorm that occurred around sunset is analyzed and simulated in the current study, as it provides a well-documented SURF event with apparent urban impacts. Routine weather data were obtained from the Meteorological Information Centre of the Beijing Meteorological Service, including automatic weather station (AWS) observations and radar reflectivity from the S-band radar at the Beijing Observatory (BJO; Fig. 1b). Concurrent 2-m temperature T and specific humidity q; 10-m wind direction and speed V; and rainfall amounts were collected at 15-min intervals from 150 AWS sites in the study area (Fig. 1c). Distances between the AWS sites average 3 and 5 km in the urban and rural areas, respectively, and all stations within RR 4 were assumed to be "urban" in the following analyses. Temperature and wind speed observations were interpolated to grid points following Cressman (1959) for easier comparison with model output parameters.

b. Model description

The WRF NWP system at IUM was used in the study, along with its version of WRF-BEP, herein referred to as uWRF. The uWRF computational domain (d02; Fig. 1a) has 50 vertical levels of varying depth, with 13 below 1 km to provide a high resolution within the PBL. Its horizontal grid resolution is 3 km, with 550 × 424 cells centered on urban Beijing. This domain is embedded within the larger IUM operational 9-km WRF Model domain (d01), which covers all of China with 649 × 400 grid cells and 50 vertical layers.

The following WRF parameterization options were used in both domains, based on evaluations by Fan et al. (2009, 2013)

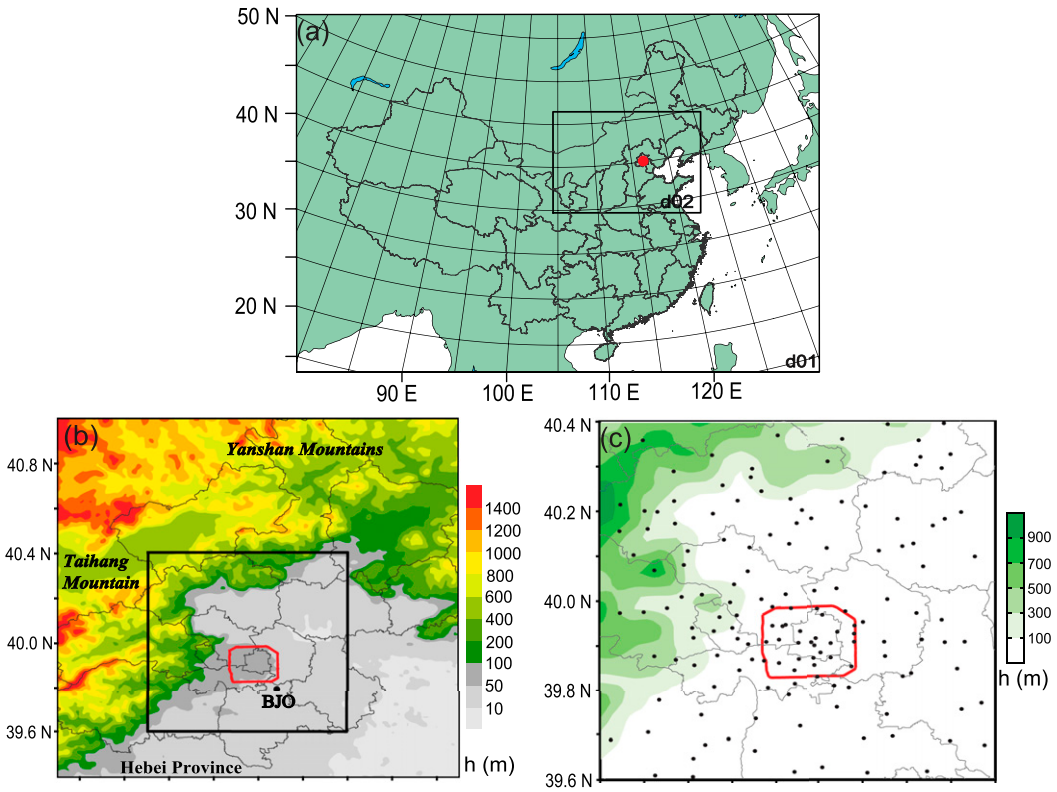

FIG. 1. Maps of the (a) outer 9-km (d01) and inner 3-km (d02; black-outlined rectangle) WRF domains, with provincial boundaries (irregular black lines) and observational study area (red dot). (b) The greater Beijing and surrounding region, with topographic heights h (m; color shading), city districts (gray lines), observational study area (black-outlined rectangle), RR 4 (red line), and Beijing Observatory (BJO; black dot). (c) Observational study area with AWS observational sites (dots) and topographic heights h (m; green shades).

of results from past 9-km WRF ensemble forecasts for Beijing: Thompson et al. (2004) microphysics; Mlawer et al. (1997) Rapid Radiative Transfer Model (RRTM) longwave radiation; Dudhia (1989) shortwave radiation; and BouLac PBL (Bougeault and Lacarrere 1989), a turbulent kinetic energy (TKE) closure. The Kain–Fritsch cumulus parameterization (Kain 2004) was used only in d01.

The Noah land surface parameterization (Ek et al. 2003) was used to simulate soil moisture and temperature in four layers for all surface grid areas in d01 and for the nonurban fractions of d02 urban cells. The BEP parameterization was used for the urban fractions of d02 cells. Resulting fluxes within mixed land-use grid cells were blended together (based on fractional coverage) to produce an effective flux used to calculate an effective 2-m temperature; see Martilli et al. (2002) for details. BEP does not overparameterize building barrier impacts by treating the entire urban area as a single solid object [as done in Bornstein et al. (1993)], an approach that thus does not allow for the parameterizations of the wind flow between urban structures. BEP also does not parameterize a city by only treating it as only as a rough surface (as in Noah and SLUCM). It rather parameterizes urban areas as a more realistic porous flow media, which produces more accurate reductions of urban 10-m and PBL wind speeds (Martilli et al. 2002). This technique has been long used in engineering fluid dynamics (e.g., Wilson and Shaw 1977; Ayotte et al. 1999), and Salamanca et al. (2010) showed that the BEP urbanization scheme produces more accurate UHIs.

All 2D gridded surface-energy balance parameters (e.g., albedo, emissivity, and urbanized surface area fractions) required for the Noah or BEP schemes for the current simulations are obtained for each urban and rural land-use class from default WRF lookup-table values for urban areas (Table 1). While not specific to Beijing, the values are generally reasonable (Oke 1987, 1988). Its 5% urban albedo α, however, is low by about a factor of 2 (Bailey et al. 1997), consistent with the Beijing flux tower observations that likewise show an α of about 0.1 (Miao et al. 2012). The current underestimation of urban α will thus increase our simulated WRF urban air temperatures (Krayenhoff and Voogt 2010), producing an overestimation of UHI intensity. If we had noticed the lookup-table error and had used a higher α, our UHI would have decreased, thus reinforcing our results of no UHI initiation of convection. Evaluation of predicted versus observed early evening UHI values (discussed in the results section) shows that both values were similar and weak. Most important, the thunderstorm precipitation in our case occurred at about 2000 local standard

TABLE 1. Energy parameters as a function of building facet, but as independent of building category.

Parameter facet	Heat capacity (10^6 J m^{-3} K^{-1})	Thermal conductivity (J m^{-1} s^{-1} K^{-1})	Surface albedo (—)	Surface emissivity (—)
Walls	1.75	1.5	0.05	0.98
Roofs	1.75	1.2	0.05	0.90
Ground	1.75	1.5	0.05	0.98

time (LST), a time when solar energy impacts had been minimal for several hours.

For the current research effort, two simulations were carried out. The "Urban case" used the high-resolution (30-m pixel size) *Landsat-5* TM-derived land-use classification in Liu et al. (2015) for the observational study area (Fig. 1c). These data are provided to the Noah and BEP algorithms, with their input gridded percentages for each rural and urban land-use category, respectively, in Fig. 2a. The number of classes was expanded from the original 18 in Noah to include three new BEP urban types (i.e., low- and high-density residential and commercial), which replaced the single Noah urban class 1. Note that the high-density urban type is centered within RR 4 and that the other two classes extend out from this area to the northwest and northeast of this central core. The prescribed distribution of building heights for each urban class is given in Table 2.

For the "NoUrban" simulation, the areas of all three urban classes within the GBA were replaced by cropland (Fig. 2b), with the central replacement area occupying about 30 by 30 horizontal grid points. Cropland is the current dominant land use surrounding Beijing (see Fig. 2a) and the class that occupied the area upon which the city developed. This replacement procedure has been used in most similar urban-impact case studies (e.g., Shem and Shepherd 2009). The area of urban Beijing turned into cropland in the NoUrban simulation is hereinafter referred to as nonurban Beijing.

For the current research effort, output from the (continuous) operational IUM WRF forecast system provided the 3-km initial conditions (ICs) and boundary conditions (BCs) in an offline, one-way feedback mode for both the Urban and NoUrban simulations. The simulations used assimilated data from the AWS sites, S-band radar, ground-based global positioning system meteorology network, radiosondes, and aircraft meteorological data relay system. The simulations were warm started at 1400 LST (=UTC + 8 h) and run for 10 h, with the operational 3-km WRF-SLUCM fields at 1400 LST used as the ICs for both the Urban and NoUrban d02 simulations. The warm-start procedure minimizes the urban impacts from SLUCM to the now rural PBL, because they quickly dissipate as a result of PBL turbulence. For the Urban case, the urban impacts are rapidly augmented and spread throughout the PBL by the turbulent transfer mechanisms associated with the multilevel BEP urbanization scheme.

c. *Model evaluation and graphics*

Quantitative evaluation of the Urban-case results against observations involved the following AWS data from the

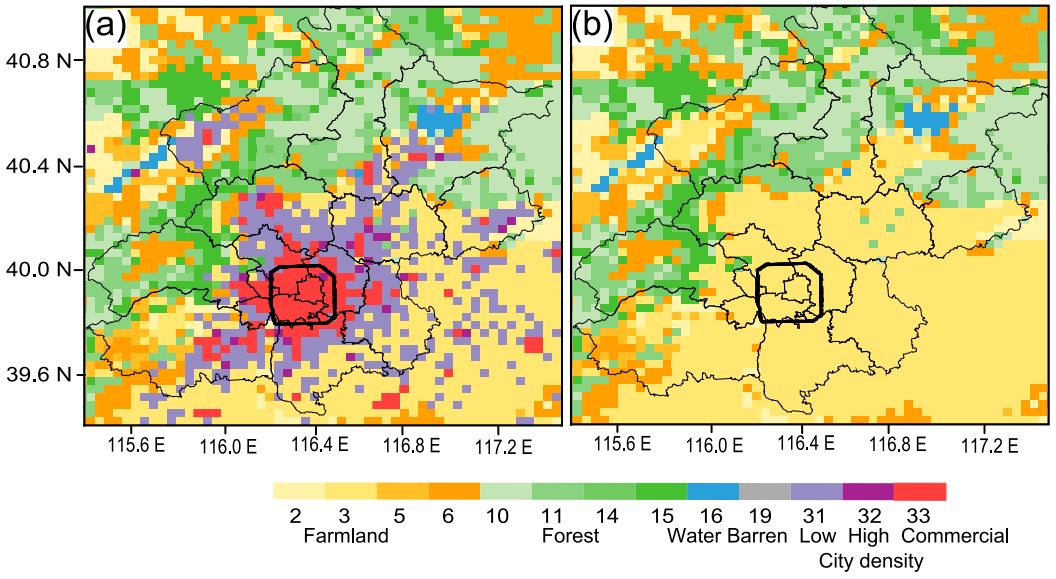

FIG. 2. Noah land-use classification maps for the greater Beijing area of Fig. 1b for the (a) Urban and (b) NoUrban WRF simulations. Class-1 urban pixels have been replaced by three new urban classes (31–33), RR 4 is the black-outlined square, and city district lines are shown by thinner black lines.

TABLE 2. Building heights h (m) and percentages (%) for each urban category.

Category h (m)	Commercial (%)	High-density residential (%)	Low-density residential (%)
5	—	—	15
10	—	20	70
15	10	60	15
20	25	20	—
25	40	—	—
30	25	—	—

pre-precipitation period (1500–1700 LST): 2-m T and q and 10-m V. All statistics are domain averages over the observational study area (Fig. 1c), while urban versus rural accuracies are qualitative estimates from observed versus simulated spatial patterns. The statistics include bias, root-mean-square error (RMSE), and hit rate (HR; Schlunzen and Katzfey 2003); HR is the fraction of model predictions within prespecified error bars, herein set as 1°C for T, 1 m s^{-1} for V, and 1 g kg^{-1} for q, being the "strict" accuracies suggested by Cox et al. (1998). Surface precipitation predictions, however, are evaluated by true skill statistic (TSS) values, also known as the Hanssen and Kuipers discriminant. It incorporates "correct rejections" and provides a holistic measure of forecast performance (for additional details see https://cawcr.gov.au/projects/verification/).

The component of the simulated horizontal-wind V projected into the plane of vertical cross sections (V_c) was calculated as follows:

$$V_c = u\cos\alpha + v\sin\alpha, \tag{1}$$

where u and v are the west–east and south–north components of V, respectively, and α is now the angle between the vertical plane and the west–east direction. In all cross sections with wind vectors, the plotted horizontal component is V_c, whereas the vertical component is 5 times w (for clarity).

3. Observed results

a. Observed synoptic conditions

Near-surface synoptic conditions at 1400 LST 22 July (Fig. 3a) show a synoptic-scale convergence line over the GBA with synoptic-scale high pressure centers to its northwest and southeast. The convergence resulted from the northwesterly and southeasterly flows from the two highs, respectively. By 2000 LST the line had just passed the GBA (Fig. 3b). This convergence line will be shown below to be associated with the precipitation area that subsequently passed over Beijing.

The only available rawinsonde sounding was at 2000 LST (Fig. 4) at BJO, located about 50 km southeast of the center of Beijing (Fig. 1b). The sounding, taken just after the storm passed Beijing, shows the lifting condensation level (LCL) at 1023 m, convective condensation level (CCL) at 1219 m, and level of free convection (LFC) at 2146 m. Dry-adiabatic conditions exists up to the LCL, with conditionally unstable conditions (temperature lapse rate of about 6°C km^{-1}) then up to the tropopause. Its CAPE value to 12 km was 816 J kg^{-1}, indicative of weak convective conditions for Beijing (Sun et al. 2015). Wind speeds were small throughout the troposphere, with a peak of only 27 m s^{-1} at the tropopause. Near-surface winds were southwesterly while those above 4.5 km were westerly, indicative of a normal midlatitude westerly shear at these elevations. Between these layers was a weak northerly flow transition zone of about 2 m s^{-1} at 1.5 km. The weak synoptic forcing of this case allows for mesoscale features, such as those from urban areas, to become more evident (Pielke 2013).

b. Observed winds and precipitation

The observed 1800 LST S-band radar reflectivity Z_r at an elevation of 1.5 km showed a convective system in the mountain areas northwest of Beijing (figure not shown). An hour later (Fig. 5a), the system moved into the GBA, with the most intense echoes closest to the Beijing urban area. By 2000 LST (Fig. 5b) the system was more organized and had moved

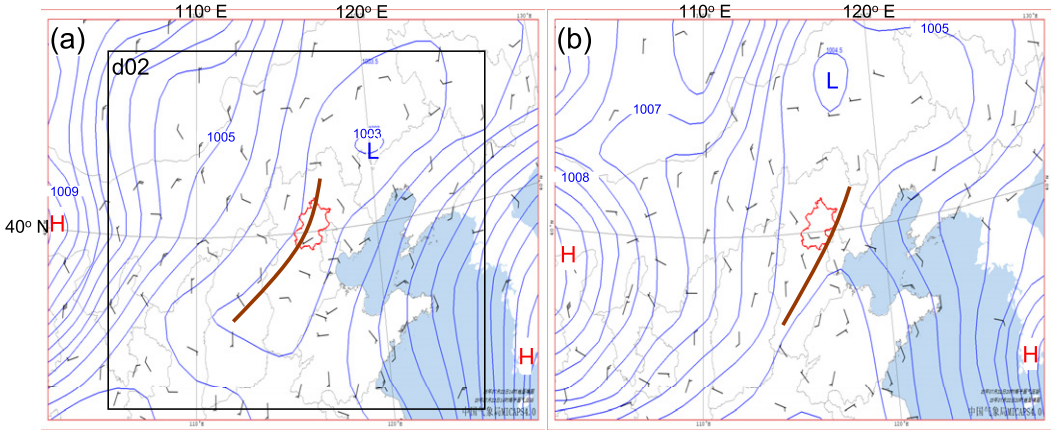

FIG. 3. CMA synoptic sea level charts on 22 Jul showing pressure (0.5-hPa increment) and wind velocity (1 full barb = 4 m s^{-1}) for (a) 1400 and (b) 2000 LST. Also shown are the greater Beijing area (red outline) and subjectively located synoptic flow convergence lines (brown).

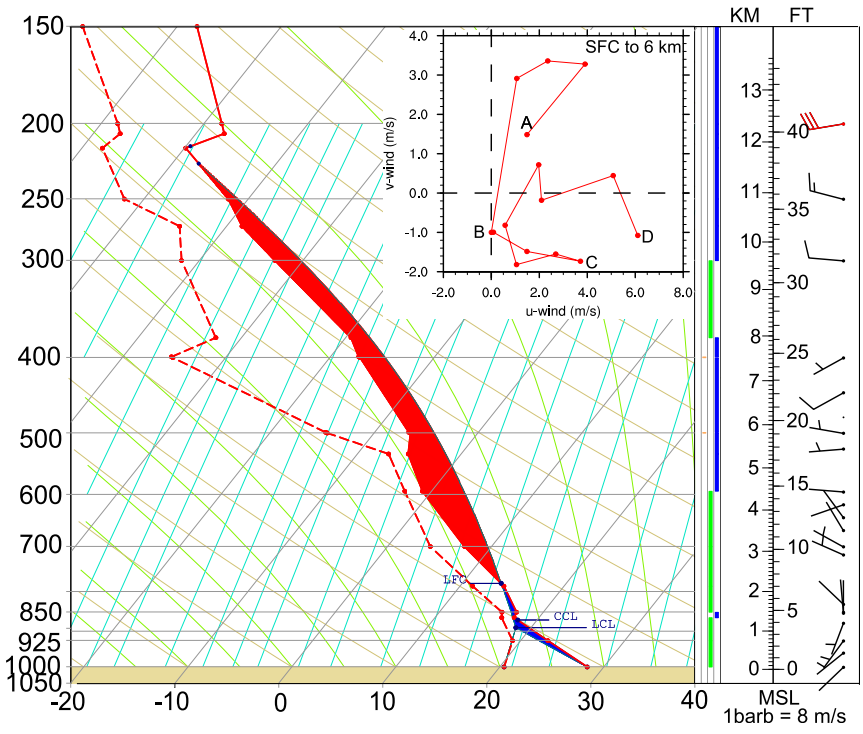

FIG. 4. Observed lowest 15 km of rawinsonde at BJO (location in Fig. 1b) at 2000 LST 22 Jul 2015. Temperature (°C; solid line), dewpoint temperature (°C; dashed line), and wind velocity (1 full barb = 8 m s^{-1}) are plotted vs pressure (hPa). Points A, B, C, and D coincide with the surface, 1.5, 3, and 6 km, respectively, and the LFC, CCL, and LCL are discussed in the text.

southeastward toward the city, with its strongest echoes just reaching Beijing. After another hour (Fig. 5c) the strongest echoes had moved even farther ahead of the stratiform region and had bifurcated around the city. Note that the main convective line behind these echoes shows no significant forward movement in the 2 h since Fig. 5a, indicative of its strong topographic forcing.

The concurrent 2000 LST location of the regional surface convergence line from Fig. 3b shows it about 120 km southeast of the 1.5-km-level radar echo centerline (Fig. 5b). A more detailed spatial and temporal (24 min) echo patterns during the bifurcation period (1948–2036 LST) is shown in Figs. 5d–f. The strongest echoes at 1948 LST (Fig. 5d) are at the western mountain edge north of Beijing. A slowing of the storm section upwind of the center of the city is visible, consistent with the upwind urban impacts of NYC on the radar echoes in Bornstein and LeRoy (1990). The storm moves to the northern urban edge at 2012 LST (Fig. 5e), where it shows partial bifurcation, with complete bifurcation apparent by 2036 LST (Fig. 5f).

Concurrent observed AWS surface precipitation data show a similar evolution as the radar echoes. The single cell north of Beijing at 1915 LST (Fig. 6a) moved to its northeast corner by 2000 LST (Fig. 6b), with several smaller centers around the main cell. By 2015 LST (Fig. 6c) the storm core has bifurcated, with one cell on either side of the city. During the next 15 min the western cell intensified, while the eastern one fragments (Fig. 6d). By 2100 LST (Fig. 6e), one cell each is located southeast and southwest (stronger of the two) of Beijing, while a northern fragment remained behind and weakened. By 2115 LST (Fig. 6f) both bifurcated cells have weakened.

The observed AWS storm-total accumulated precipitation during 1800–2200 LST (Fig. 7) shows a maximum north of Beijing; reduced accumulation directly south of that, but still north of the city; and bifurcated maxima on both sides of Beijing. These results are consistent with those from the climatological study of Dou et al. (2015), which focused on storms passing south to north across Beijing.

Observed AWS 10-m winds at 1900 LST (Fig. 8a) show a southeasterly regional flow in the southeastern part of the domain. A separate more organized regional southwesterly flow in the southwestern part of the domain bifurcates around Beijing. While the storm was still over the mountainous area northwest of the city (outside this domain), its 10-m northwesterly outflow has moved into the area, producing a local outflow gust front where it meets both regional flows. The concurrent divergence pattern (Fig. 8b) showed a strong convergence (up to $-6\ 10^{-4}\,s^{-1}$) along the outflow front, with equally strong divergence behind it.

By 1945 LST, the gust front was over Beijing (Fig. 8c). The now stronger northwesterly flow behind it, and the southeasterly flow ahead of it, both bifurcate around the city, breaking the front. Concurrent divergence values (Fig. 8d) show a now weaker (4.5 vs $6.0 \times 10^{-4}\,s^{-1}$) maximum behind the front. The convergence maxima on both sides of Beijing were also that much weaker, while the urban core shows a small area of weak

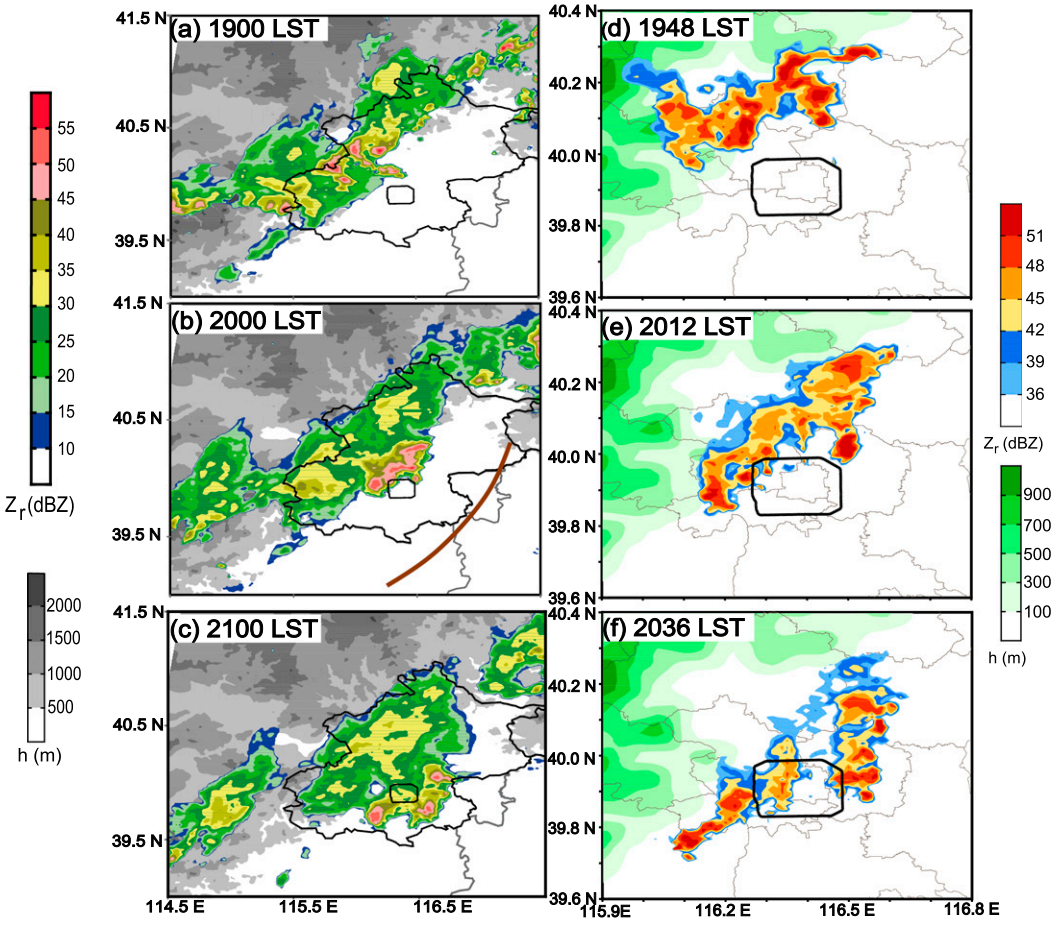

FIG. 5. Observed (1.5-km level) S-band radar reflectivity Z_r (dBZ; colors) at (a) 1900, (b) 2000, and (c) 2100 LST 22 Jul for the greater Beijing area and at (d) 1948, (e) 2012, and (f) 2036 LST for a zoomed-in area centered on urban Beijing. The black-outlined squares are RR 4, and the brown line in (b) is the synoptic convergence line of Fig. 3. Topography is shown in grays in (a)–(c) and greens in (d)–(f).

divergence ($1.5 \times 10^{-4}\,s^{-1}$). By 2000 LST (Fig. 8e), the gust front had re-formed southeast of Beijing, with even faster northwesterly winds and with the still slower southeasterly flow.

Placement of the concurrent 2000 LST AWS precipitation pattern from Fig. 6b on the flow pattern of Fig. 8e reinforces the above conclusion that the convergence zone is the thunderstorm outflow gust front. The high speeds over Beijing thus result from outflow from the strongest precipitating cell at the northwest edge of the city. The locations (relative to the front), as well as the magnitudes of the maximum convergence and divergence areas (Fig. 8f), remain unchanged. Note that the concurrent lowest-level BJO radiosonde (location shown in Fig. 8e) southwesterly winds in Fig. 4 are consistent with the prefrontal winds near that site.

4. Simulation results

a. *Near-surface winds and temperatures before precipitation event*

At 1700 LST, before the storm reached Beijing, the NoUrban-case regional 10-m wind vectors (Fig. 9b) show a speed ($>3\,m\,s^{-1}$) southeasterly flow in the southeastern part of the domain. This shifts to a lower-speed (about $2\,m\,s^{-1}$), generally southerly flow over the rest of the domain, with a return to higher speeds over the western mountains. Corresponding Urban-case values (Fig. 9a) show a similar overall pattern, but with a clear speed minimum ($<1\,m\,s^{-1}$) over Beijing and a tendency for a divergent flow around the city.

The minimum is also seen in the differences in Fig. 9d, which show a maximum reduction of about $1.5\,m\,s^{-1}$ over central Beijing, along with generally smaller reductions over the localized commercial areas north of the city (see Fig. 2a). Given the simulated southerly flow direction south of Beijing, the largest reductions are generally over and downwind of the city in an arc-shaped pattern. This location is indicative of advective effects, and perhaps with a downwind bifurcation of low speed momentum. The corresponding 10-m AWS wind speed observations (Fig. 9c) show that the Urban-case simulation reproduced the urban speed minimum, as well its downwind impact. The minimum is due to the correct parameterization in uWRF-BEP of both the urban increased z_0 and building-barrier impacts. The observed vectors in Fig. 9c show a

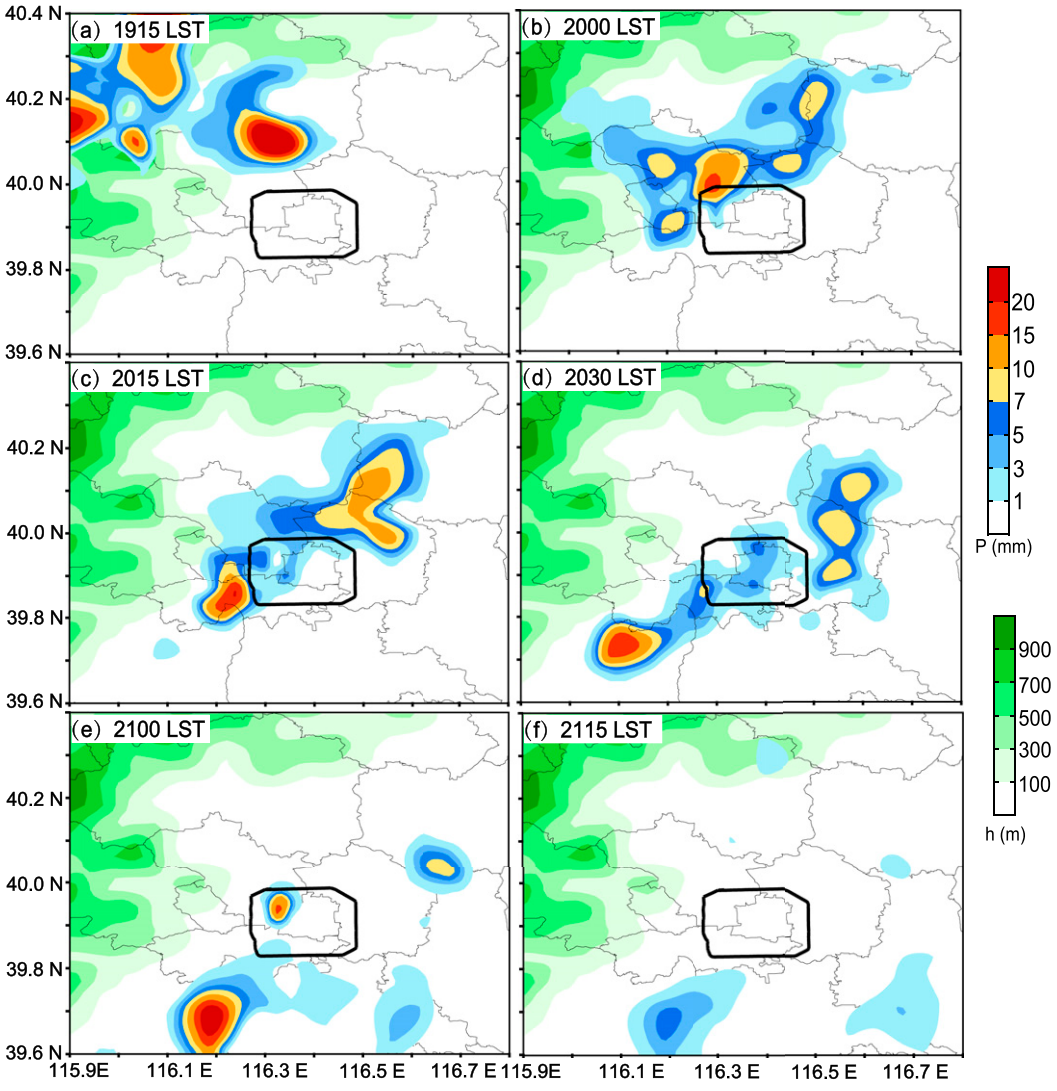

FIG. 6. Observed 15-min AWS surface precipitation P values [mm (15 min)$^{-1}$; color shades, with nonuniform intervals] over the greater Beijing area at (a) 1915, (b) 2000, (c) 2015, (d) 2030, (e) 2100, and (f) 2115 LST 22 Jul.

somewhat stronger divergent flow around Beijing than the simulated ones.

Concurrent NoUrban-case 2 m temperatures at 1700 LST (Fig. 10b) show minimum values (as expected) over the higher mountains west of nonurban Beijing as well as maxima values to the south (also expected) and in the basin east of the mountains. Corresponding Urban-case values (Fig. 10a) show a similar pattern in the nonurban areas around Beijing. A near uniform urban temperature exists within RR 4 of about 31°C. Concurrent differences (Fig. 10d) show a near-uniform weak UHI (<0.5°C), arbitrarily defined herein as the Urban-case minus NoUrban-case values within RR 4. The weakness resulted from the regional cloudiness on this day. Concurrent observed AWS values (Fig. 10c) show that while both simulations captured the maximum values in the basin east of the mountains, they both overestimated the nonurban values in the western domain by up to 2°C. The overestimation thus probably results from the large-scale lateral BCs and not from the urbanization scheme in uWRF.

Evaluation of the UHI at this time is not so clear, that is, the observations in Fig. 10c show the air north of Beijing warmer than that over the city by about 0.5°C, while a west to east comparison through Beijing shows a uniform temperature across the city within RR 4, with an observed UHI of < 0.75°C. The differences between the two WRF simulations (Fig. 10d) likewise show a uniform temperature increase (i.e., UHI) within RR 4 over the city in the Urban-case of about only $<$ 0.5°C. Use of a better (i.e., higher) urban albedo in the Urban-case simulation (as discussed above in the methodology section) would have produced an even lower simulated UHI. The observed and simulated estimates are thus similar and both below 1.25°C, the climatological value that Dou et al. (2015) found necessary for UHI initiation of thunderstorms over Beijing.

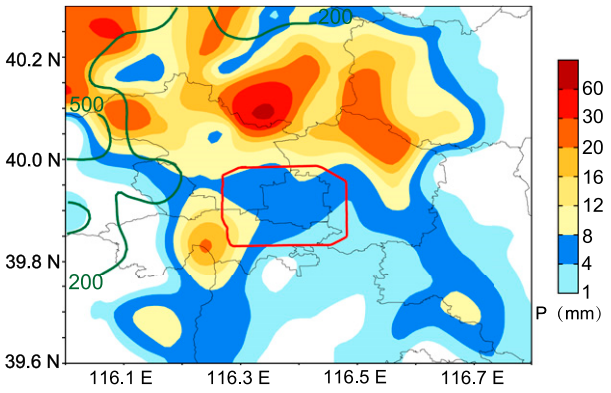

FIG. 7. AWS observations on 22 Jul of total accumulated (1800–2200 LST) precipitation P (mm; color shades, with nonuniform intervals). Also shown are the key topographic heights of 200 and 500 m (green lines) and RR 4 (red square).

Figure 11 shows the vertical distribution of the simulated UHI values at 1700 LST, defined as temperatures from Urban case minus NoUrban case. The section is along the northwest to southeast line in Fig. 14c. Results show a weak near-uniform UHI value (<0.3°C) over Beijing, consistent with both the 2-m WRF differences of Fig. 10d and AWS observations of Fig. 10c. This value remains consistent to a height of about 1.3 km, which can be used to define the PBL depth over Beijing at this time. The UHI at the surface and at the PBL top are both advected to the area northwest of the city, implying that the concurrent near-surface southeasterly flow of Fig. 9a extends throughout the PBL. A layer of cooler urban air (<0.25°C) exists above the PBL, consistent with the urban cool island or ''cross over layer'' first identified in observations over NYC by Bornstein (1968). In summary, the current UHI value is well below the 1.25°C value that the observations of Dou et al. (2015) identified as required for possible thunderstorm initiation over Beijing, and the results are in agreement with Bornstein (2011) who first hypothesized that weak UHIs would produce bifurcating storms.

Table 3 summarizes the evaluation of the mean (averaged over the entire observational study area) prerainfall (1500–1700 LST) uWRF results against the 150 corresponding AWS observations. The temperature bias is small (0.27°C), and its RMSE is about 1°C, while its HR is moderate at 0.67. The specific humidity bias is also small ($-0.25\,\mathrm{g\,kg^{-1}}$), while its RMSE is $0.75\,\mathrm{g\,kg^{-1}}$. Its relative errors are thus both excellent, and its HR is 0.83. While the speed bias of $0.86\,\mathrm{m\,s^{-1}}$ and RMSE of $1.6\,\mathrm{m\,s^{-1}}$ are not excessive, the low observed mean speeds indicate large relative errors.

These results, in combination with the speeds of Fig. 9a versus Fig. 9c, imply that the speed errors in Table 3 must be mostly at the rural sites. The comparably small HR (of 0.57) for V is due to the complex flow structures within urban areas, which cannot be perfectly simulated by the uWRF building parameterization. In summary, prefrontal near-surface conditions in the Beijing area were generally well depicted by uWRF.

b. Precipitation event

The simulated Urban-case precipitation area at 1900 LST (not shown) was over the mountain areas northwest of Beijing, but 45 min later it was just north of the city (Fig. 12a vs Fig. 6a). Absent an urban building barrier effect, the NoUrban-case precipitation (Fig. 12b) has moved too far southward to a position over northeastern nonurban Beijing. The Urban-case precipitation diminished by 2000 LST (Fig. 12c) as it moved farther southward and started to bifurcate around the city. The bifurcation is more advanced by 2015 LST (Fig. 12e), while the cells on both sides of the city have increased in aerial extent. By 2030 LST (Fig. 12g) both cells have mostly passed the city and the eastern cell has started to bend in behind Beijing. During the same 45 min (Figs. 12d,f,h), the NoUrban-case cells pass over nonurban Beijing and fragment.

Comparison with the concurrent AWS observations (Fig. 6), shows that uWRF has captured the main features of the life cycle of the bifurcating storm. It has, however, overestimated its aerial extent north of Beijing (Fig. 12a). As the concurrent NoUrban-case results (Fig. 12b) also overestimate this aerial extent, the same large-scale lateral BCs for both simulations are probably the source of the error. The Urban-case simulations also, however, move the eastern cell too fast southward and overestimate its strength along its bifurcating trajectory.

The total accumulated precipitation for the Urban case during 1800–2200 LST (Fig. 13a) shows areas with strong rainfall north of Beijing, lower precipitation over the northern half of the city, strong bifurcation, and a rain shadow south of the city. The northern maximum is of the same magnitude (60 mm), but more organized than, the observations of Fig. 7, while the uWRF bifurcation areas are larger in both extent and magnitude (50 vs 20 mm) than the observations, especially in the eastern cell. The bifurcation angle (i.e., between the centerlines of each cell) is smaller than the observed value of Fig. 7. This underestimation results from the fact that the Urban-case eastern cell is too weakly bifurcated during its trajectory around Beijing, perhaps because of underestimation of its WRF lookup-table building densities.

The corresponding NoUrban accumulation results (Fig. 13b) also overestimate the areal extent of the northern accumulation region, again implying that the input lateral BCs (and not uWRF) is the source of this error. This simulation also moved the storm directly over nonurban Beijing, and it thus does not reproduce the observed bifurcation areas. The simulated differences (Fig. 13c) also clearly highlight the bifurcated rain areas as well as the reduced rainfall region over central Beijing.

The area of minimum accumulation over the northern half of Beijing in both the observations (Fig. 7) and uWRF results (Fig. 13a) implies that the storm first weakened in a divergent north to south flow around the city (discussed below). It then restrengthened in lateral convergence zones, in which the bifurcated flows converged with the undisturbed flows on both sides of the city, again in agreement with bifurcating storms over NYC in Bornstein and LeRoy (1990). The BEP scheme is thus able to first impact the storm while its main precipitating area was still north of Beijing (Fig. 13a vs Fig. 13b) and then to

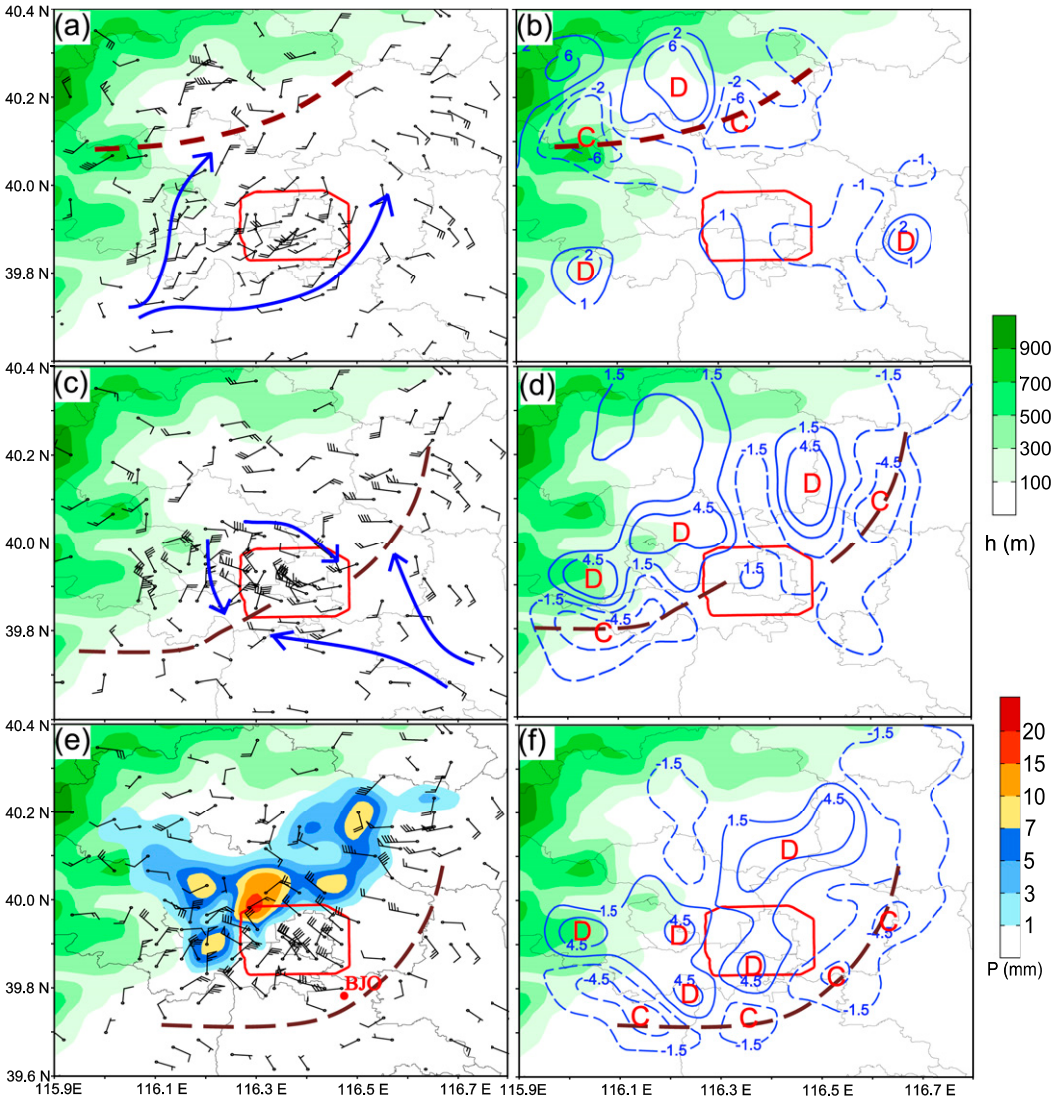

FIG. 8. Observational study area (Fig. 1c) 10-m AWS wind speeds (1 full barb = 1 m s^{-1}) at (a) 1900, (c) 1945, and (e) 2000 LST 22 Jul and their corresponding diagnostic 10-m divergences (10^{-4} s^{-1}) at (b) 1900, (d) 1945, and (f) 2000 LST. Also shown are BJO [red dot in (e)], topographic heights h (m; green shades), and maximum negative convergence (C) and positive divergence (D) centers as well as subjectively located local storm outflow gust fronts (brown dashed lines), local flows (blue arrows), and observed precipitation [mm (15 min)$^{-1}$; color shades, with nonuniform intervals] in (e).

bifurcate its precipitation, even with its apparent too weak building densities.

Quantitative evaluation of the Urban-case precipitation results (Table 4) shows its TSS values as a function of five prescribed threshold total accumulation amounts P. The TSS value for precipitation occurrence ($P \geq 0.1$ mm, regardless of magnitude) is high at 75%, as uWRF correctly predicted rain anytime during the event at 126 of 157 sites. It also predicted rain at 29 sites where no rain occurred, while it failed to correctly predict rain at only two sites.

Simulation accuracy decreased with increased P threshold, and thus uWRF did poorest (only 3% accuracy) for the highest threshold ($P \geq 50$ mm), beyond which uWRF matched observations at only one site and overpredicted at 27 others. Overprediction dominance relative to underprediction (as percent of cases) is seen for all P thresholds. Its value increased to 90% with increasing P value, while underprediction peaked at only 16% for $P \geq 10$ mm. Overprediction was especially strong in the two bifurcating cells (Fig. 13a vs Fig. 7).

c. PBL structure

The 1900 LST NoUrban-case winds at the 10-m level (Fig. 14b) show that the storm outflow confluence zone has entered the domain and is at the northwest corner of nonurban Beijing, bringing a strong (up to 9 m s^{-1}) northerly outflow. A local divergent vortex exists southwest of nonurban Beijing,

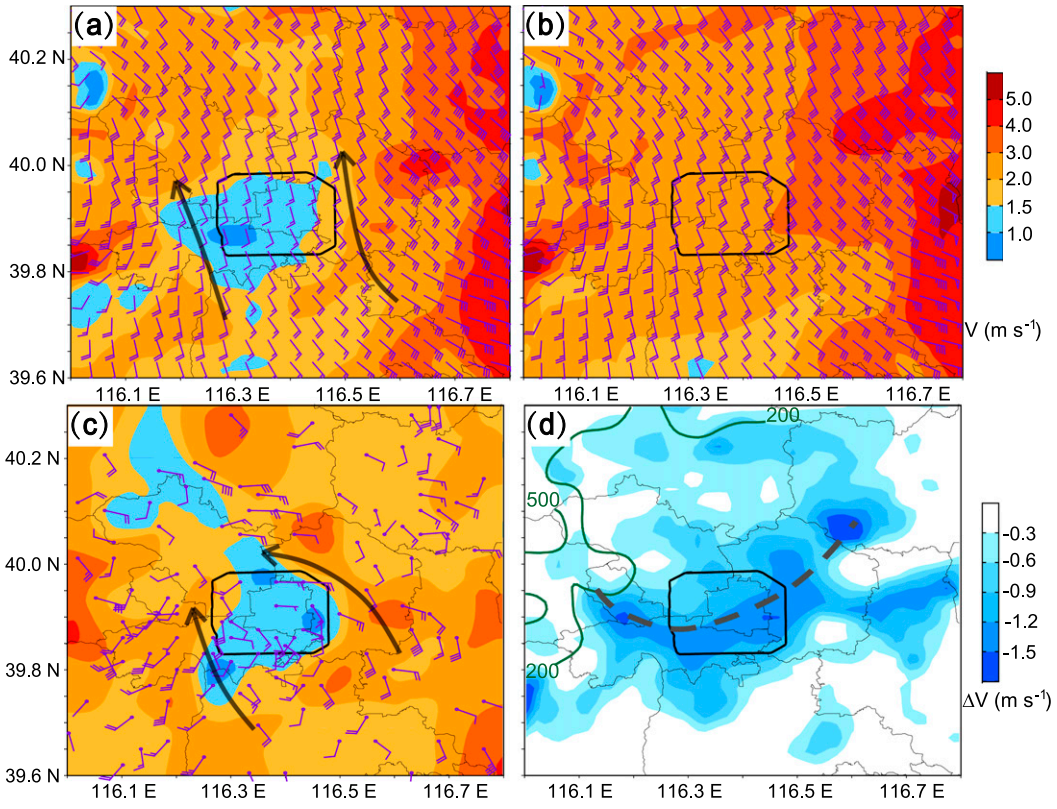

FIG. 9. Simulated 10-m wind vectors (1 full barb = 1 m s^{-1}) and speeds (color shades; m s^{-1}) at 1700 LST 22 Jul for the (a) Urban and (b) NoUrban cases, along with (d) Urban minus NoUrban speed differences (m s^{-1}). Also shown are (c) the observed vectors and speeds. Shown in (d) are the key topographic heights of 200 and 500 m (green lines) and the dashed center line of maximum speed differences. Subjectively located flow vectors (black arrows) are shown in (a) and (c).

and the regional southeast synoptic flow is only about 3 m s^{-1}, as it was 2 h previous in the NoUrban simulation of Fig. 9b. The corresponding Urban case (Fig. 14a) shows the confluence zone retarded by Beijing, even as it is still north of the city. Its location is thus closer to the concurrent observations of Fig. 8a than in the NoUrban case. Speeds over Beijing are reduced (as 2 h earlier in Fig. 9a) by about 1.5 m s^{-1}.

By 1915 LST, the NoUrban-case winds (Fig. 14d) show the confluence zone directly over central nonurban Beijing, with the local divergent vortex still southwest of nonurban Beijing. Corresponding Urban-case winds (Fig. 14c) show a similar pattern, but with the front still correctly retarded by the city. A tendency for divergent flow out from and around the city is seen north of Beijing.

By 1930 LST the NoUrban-case winds (Fig. 14f) show that the confluence zone has moved to the southern edge of the nonurban Beijing. In the corresponding Urban case (Fig. 14e), the confluence zone has also passed the city, but has broken into two parts, as in the nearly concurrent observations in Fig. 8c. The flow continues to show a tendency to diverge around Beijing, which will be seen below to impact its corresponding w fields. The simulated front has, however, moved about 15 min quicker than in the observations of Fig. 8e.

The simulated Urban-case precipitation patterns in Fig. 14 also correctly track the storm movement toward Beijing up to 1930 LST (Fig. 14e). That position is consistent with its simulated location nearer (but still north of) the city at 1945 LST in Fig. 12a. The storm has not yet reached Beijing at 1930 LST, but its outflow already shows divergent flow around the city. This implies that the subsequent bifurcated precipitation 30 min later (Fig. 12c) resulted as the storm followed the already established divergent flow pattern of Fig. 14e.

Vertical cross sections of projected horizontal velocity component V_c and of w in the plane of the northwest to southeast storm movement (red line in Fig. 14c) are shown in Fig. 15. The 1900 LST NoUrban-case section (Fig. 15b) shows a northwesterly synoptic flow component from the surface to the top of the section (at 6 km) in the region just downwind of the mountains. Downwind is here defined relative to the northwesterly to southeasterly storm movement in Fig. 14. Near-surface speeds (lowest level in section is 200 m) in the northwesterly storm outflow are >10 m s^{-1}, consistent with the concurrent high speeds at 10 m in Fig. 14b.

The lowest 1 km over the flat terrain southeast of and over nonurban Beijing shows the weaker southeasterly synoptic flow of Fig. 14b, capped by a minimum speed transition zone (centered at 1.5 km) above this zone and extending to the top

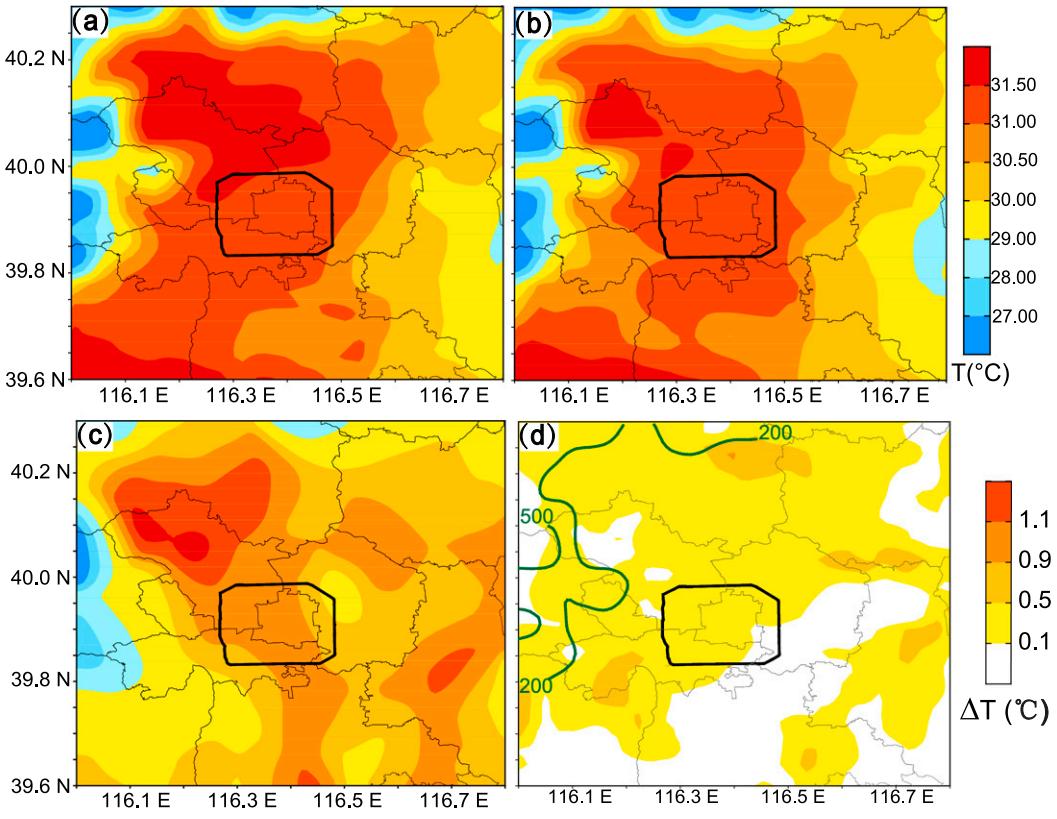

FIG. 10. As in Fig. 9, but for 2-m temperature for (a) Urban, (b) NoUrban case, (c) observations, and (d) Urban minus NoUrban case.

of the section, the opposite direction (northwesterly) synoptic flow is again present. Upward motions are triggered in the region between the western mountains and nonurban Beijing where the two near-surface flows converge, producing peak upward speeds ($>2\,\mathrm{m\,s^{-1}}$) at about 3 km. Weaker upward motions generally exist on both sides of this zone over much of the remaining domain.

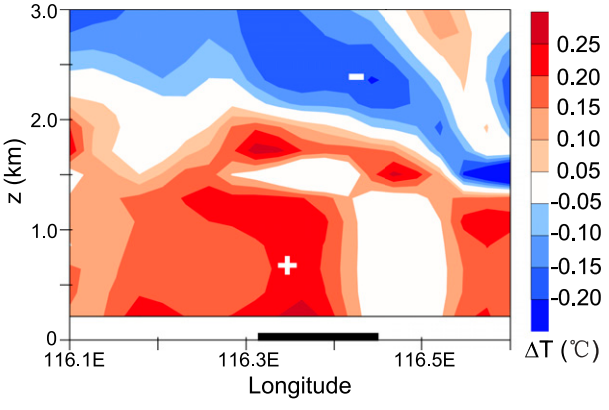

FIG. 11. Vertical cross section of UHI values (positive red areas) at 1700 LST along the northwest-to-southeast plane depicted below in Fig. 14c, where ΔT (°C) are simulated values for the Urban case minus NoUrban case.

Corresponding Urban-case vectors (Fig. 15a) generally show a similar three-layer pattern as well as the area of peak upward motion. The three vertical layers in Fig. 15 also are consistent with the observations in the lower 6 km of the (30 min later) rural BJO radiosonde (Fig. 4), except for the direction within its near-surface transitional layer (discussed above).

The Urban-case confluence zone, however, is farther upwind of Beijing than in the NoUrban case, consistent with their relative concurrent 10-m locations in Figs. 14a and 14b. Frontal retardation even before the storm reaches Beijing is again

TABLE 3. Statistical evaluation of WRF Urban-case domainwide mean value for 2-m temperature T (°C) and specific humidity q ($\mathrm{g\,kg^{-1}}$) and for 10-m wind speed V ($\mathrm{m\,s^{-1}}$) against the corresponding AWS observations during 1500–1700 LST. The bias is the average difference between the simulated (uWRF) and observed (Obs) values, RMSE is the root mean-square error, and HR is the hit rate, with inclusion criteria of 1°C for T, $1\,\mathrm{g\,kg^{-1}}$ for q, and $1\,\mathrm{m\,s^{-1}}$ for V.

	Mean values				
	Obs	uWRF	Bias	RMSE	HR
V ($\mathrm{m\,s^{-1}}$)	1.63	2.49	0.86	1.60	0.57
q ($\mathrm{g\,kg^{-1}}$)	15.62	15.37	−0.25	0.75	0.83
T (°C)	30.60	30.87	0.27	1.06	0.67

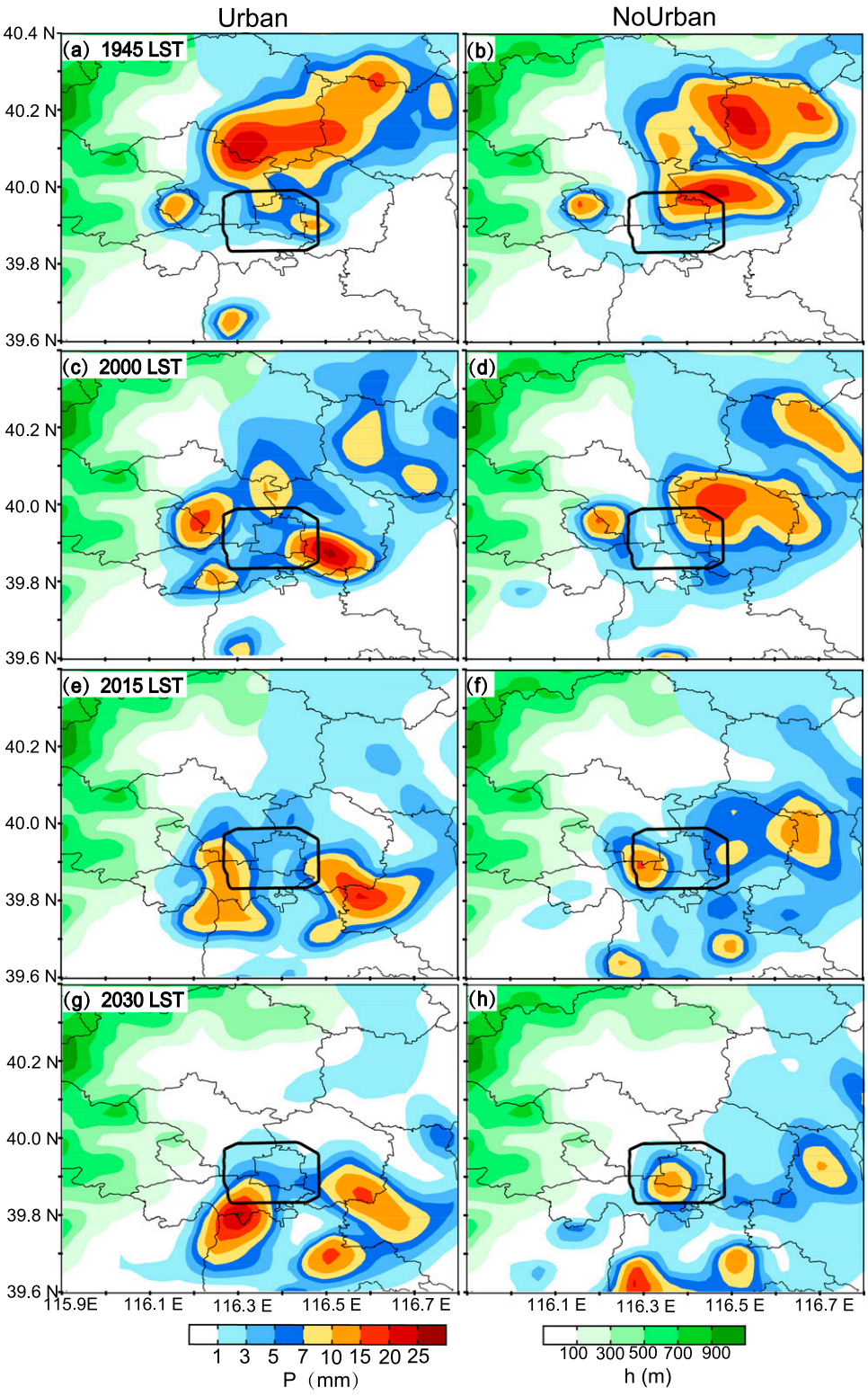

FIG. 12. Simulated precipitation values [mm $(15\,\text{min})^{-1}$] at (a),(b) 1945; (c),(d) 2000; (e),(f) 2015; and (g),(h) 2030 LST 22 Jul for (left) the Urban case and (right) the NoUrban case.

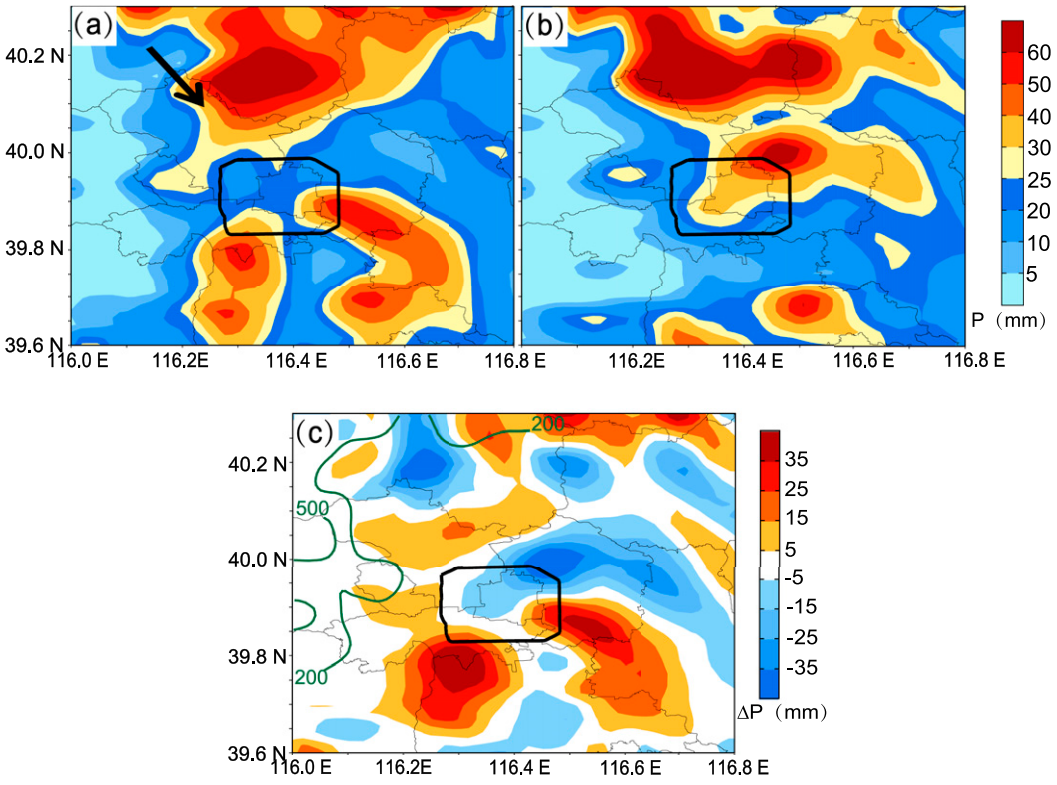

FIG. 13. Total simulated (1800–2200 LST) precipitation P (mm) on 22 Jul for the (a) Urban and (b) NoUrban cases and (c) Urban minus NoUrban differences; the black arrow in (a) shows subjectively determined direction of storm movement, and the green lines in (c) show key topographic heights of 200 and 500 m.

consistent with the observations of sea breeze and cold fronts over NYC, both at the surface (Loose and Bornstein 1977) and within the PBL (Gaffen and Bornstein 1988). Another exception is the weak (but deep) upward and then downward motions that form as the low-level flow traverses Beijing from southeast to northwest. These motions result as the flow first decelerates at the upwind urban edge (due to its large urban z_0) and then reaccelerates as it leaves the rough city, consistent with the 10-m wind speed observations in NYC of Bornstein and Johnson (1977).

The Urban-case vectors at 1930 LST (Fig. 15c) show that the convergence zone has moved to the upwind edge of Beijing and that the near-surface urban impacts of Fig. 15a are now overwhelmed by the convergence zone and its w motions. Its position is, however, consistent with its concurrent surface location at the downwind urban edge (Fig. 14e), as an area of maximum frontal upward w should be somewhat intermediate between the locations of its surface convergence and precipitation areas. This position arises as the warmer air in the southeasterly flow first starts to rise over the sloping front and then continues to rise over its sloping surface until it reaches its maximum upward w and then finally the LCL. The NoUrban-case section (Fig. 15d) shows its maximum w area directly over nonurban Beijing, also consistent with its erroneous farther southeast surface position, for the reasons just given.

The Urban-case west–east (blue line in Fig. 14d) V_c and w cross section at 1830 LST (Fig. 16a) is about 45 min before the surface front reaches Beijing and when the city is still in the generally southeasterly near-surface regional flow of Fig. 14c. The section shows that the upward motions over both Beijing lateral edges surround an area of equally strong downward motions over the city center. The peak upward w west of Beijing is at an elevation of 2 km and is twice as strong ($>0.5\ \mathrm{m\ s^{-1}}$) as the eastern peak. The NoUrban results (Fig. 16b), in contrast, show regional upward motions over most of nonurban Beijing.

TABLE 4. Number and percent of stations with correct, overestimated (o/e), and underestimated (u/e) AWS surface accumulated event precipitation from 1800 to 2200 LST. Values are given within five TSS classes, each of which is defined by a minimum event precipitation value P (mm).

	P (mm)				
Accuracy	≥0.1	≥5	≥10	≥25	≥50
TSS value	0.75	0.39	0.31	0.37	0.22
Percent of correct stations	80	38	27	13	3
No. of correct stations	126	48	31	9	1
Percent of o/e stations	18	48	57	79	90
No. of o/e stations	29	62	65	55	27
Percent of u/e stations	2	14	16	8	7
No. of u/e stations	2	18	18	6	2
Total No. of stations	157	128	114	70	30

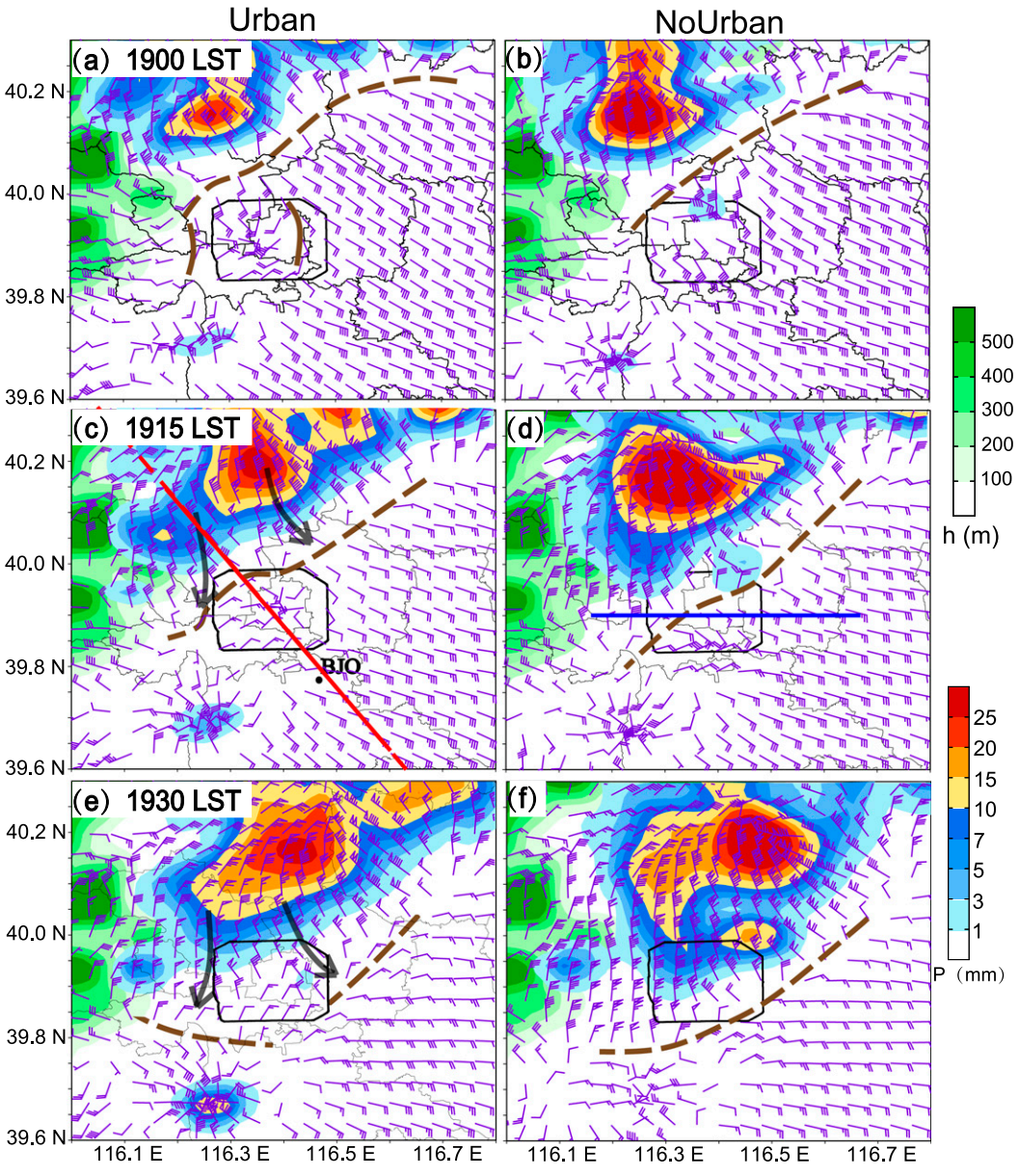

FIG. 14. Simulated 10-m wind vectors (1 full barb = 1 m s^{-1}) at (a),(b) 1900; (c),(d) 1915; and (e),(f) 1930 LST 22 Jul for (left) the Urban case and (right) the NoUrban case. Also shown are subjectively located local flows (arrows), local outflow confluence zones (brown lines), simulated 15-min precipitation amounts (mm; red and blue color shades), topographic heights h (m; green shades), and vertical cross-section planes (blue and red lines) for subsequent figures.

The eastern upward motion area in Fig. 16a is consistent with the small area of simulated 10-m convergence (30 min later in Fig. 14a) from the east–west components of the divergent flow out from Beijing. The stronger western upward motion area is likewise consistent with the likewise small area of convergence flow out of Beijing to the west; the westerly w maximum could be augmented by topographic influences.

The 1930 LST Urban-case (Fig. 16c) section is at the time when the surface front passes Beijing, which places the city in the post frontal northwesterly flow of Fig. 14e, but with the precipitation area still to its north. The section shows that the upward motions on either side of the city have increased in magnitude (>2.5 m s^{-1}) with the western maximum still centered at 1.5 km. The downward motions over the city have also increased in magnitude, reaching an absolute magnitude > 1 m s^{-1} near a height of 3 km. The corresponding NoUrban results (Fig. 16d) again move the storm too far over nonurban Beijing, consistent with the erroneous results of Fig. 12e. This location also thus causes in the erroneous strong upward motions over its center.

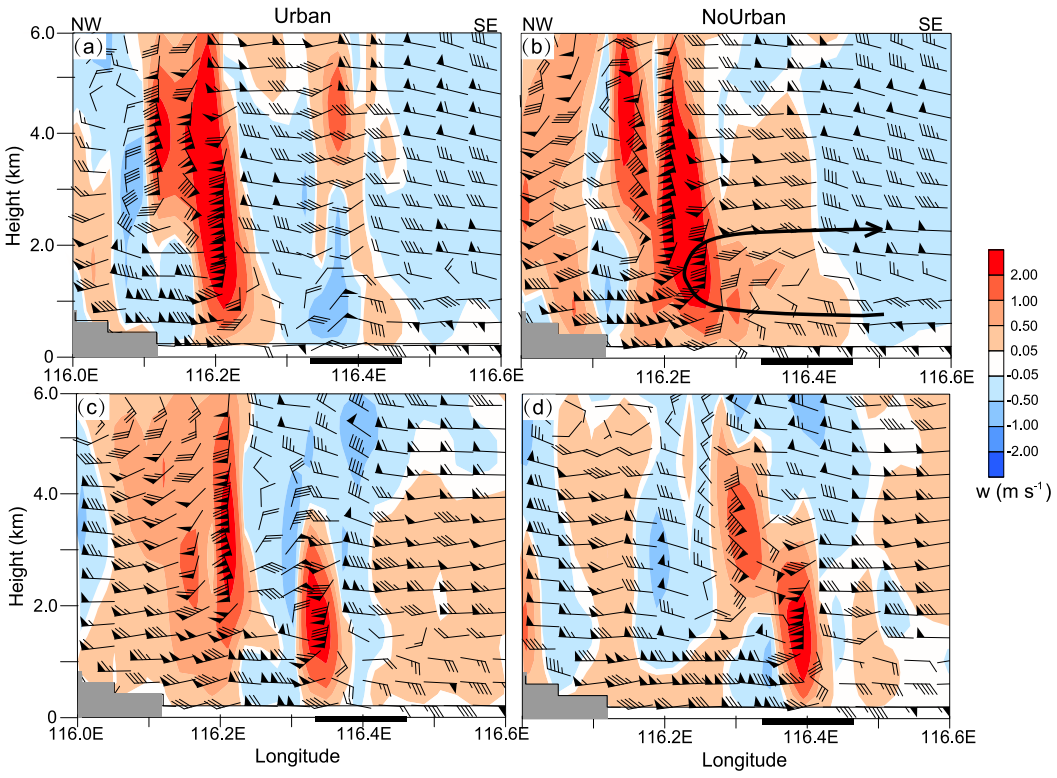

FIG. 15. Simulated wind vectors at (a),(b) 1900 and (c),(d) 1930 LST 22 Jul in the northwest–southeast (from left to right) vertical plane (red line of Fig. 14c) for the (left) Urban and (right) NoUrban cases. Vector components are vertical speed w (m s^{-1}, exaggerated by a factor of 5; color shades) and horizontal V_c (defined in the text; m s^{-1}; 1 full barb = 1 m s^{-1}). The black bar indicates the Beijing urban area, the black arrow shows the subjectively located local 2D streamline, and the gray area is topography.

The urban impacts on the w motions of Fig. 16c formed as the concurrent northwesterly storm outflow of Fig. 14e first diverges around Beijing, producing downward motions over the city center. When the divergent flows thus converge with the generally undisturbed northerly flow on either side of the city, the two lateral upward motion areas are produced.

That the storm had not yet reached Beijing in Fig. 16c again implies that the precipitation pattern of Fig. 13a resulted as the storm bifurcated as it followed the already established divergent flow pattern of Fig. 14e. The minimum precipitation area upwind of Beijing in Fig. 13a also thus resulted from the initial upwind divergence around the city, which produced the downward motions that suppressed the precipitation in this area. The two downwind lateral precipitation maxima thus subsequently formed as the storm regenerated via augmentation of the natural upward convective storm motions in the two lateral reconvergence zones.

5. Conclusions

Observations and WRF simulations were used to study the life cycle of a summer convective thunderstorm that bifurcated during its passage over urban Beijing. Results were frequently presented at 15 min intervals, a finer resolution than the 60-min increment used in most previous such efforts. The storm occurred during the Beijing SURF field study on 22 July 2015, and was analyzed by use of temperature, wind, and precipitation data from 150 AWS surface observational sites; reflectivity data from an S-band radar; and a radiosonde sounding. The study also made use of two simulations, one each with and without the city.

Specific observational results included Beijing CAPE values indicative of a weak convective storm. The simulation that included Beijing matched the main features of the observed meteorological fields, including weak 10-m winds over Beijing (<1.5 m s^{-1}) and a 2-m UHI (<0.5°C), one weaker than associated with Beijing storm initiation. The observed radar reflectivity and surface precipitation data showed a bifurcating pattern around the city, and thus a minimum accumulation over the urban core, and in a downwind urban rain-shadow area, all consistent with previous climatological observations over Beijing.

As the storm approached Beijing, but was still upwind, only the simulation with the city showed its surface forward motion retarded, in agreement with observations over NYC. As it moved forward, its simulated 10-m outflow converged with the regional flow, with both diverging around the city. Simulated vertical cross sections showed that PBL storm movement was also slowed upwind of Beijing; upward motion on the lateral sides of the city, where the bifurcated flow converged with the

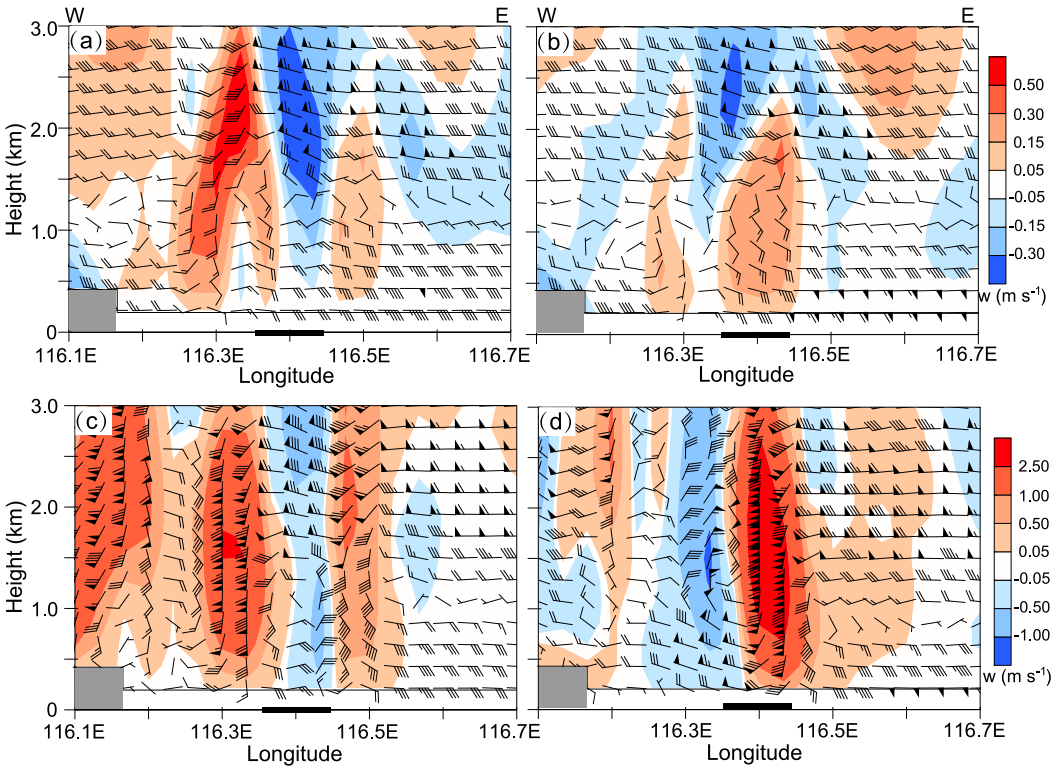

FIG. 16. As in Fig. 15, but at (a),(b) 1830 and (c),(d) 1930 LST 22 Jul in the west–east (from left to right) vertical plane (blue line of Fig. 14d).

undisturbed background flow; and downward motion over its core to 3 km.

The bifurcated flow pattern thus provided a preexisting pathway for the subsequently bifurcated precipitating region as it passed over Beijing. That these urban induced vertical motions reached to the model top at 6 km provides at least a partial explanation of how urban buildings can impact storms with bases far above their rooftop levels. These two results represent new understandings of how urban areas can impact the dynamics of such moving summer convective storms.

The observed and simulated precipitation area initially weakened upwind of the city due to the divergence (and hence downward motion) in that area, which produced an area of minimum accumulation just upwind of Beijing. The observed and simulated precipitation area then split around the city via the preexisting flow bifurcation. They subsequently restrengthened in the preexisting convergence areas (with their resulting upward motions) on both sides of Beijing. The resulting precipitation pattern and amounts from this series of events were reasonably well simulated only when urbanization was included in the model, except for underestimated values at the few stations with high accumulations. This result maybe partly due to the Urban-case results of a too narrow simulated downwind bifurcation angle between the two resulting cells.

The study thus represents a contribution to the evolving literature on urban impacts on summer convective storms. Additional simulations, however, are needed to overcome the limitations of the current effort. A finer horizontal grid resolution, for example, should make it possible to discern effects from urban induced pressure variations on storm evolution. Future efforts should also make use of the now available gridded Beijing urban building morphological dataset of He et al. (2019) and other urban parameters. The BEP urbanization of the current study should also be linked to the WRF Building Energy Model (BEM) urbanization option. Parametric simulations should also be carried out, for example, without the western orography and with a varying degree of urban building densities and thermal characteristics. Additional bifurcation cases could be investigated in cities of varying sizes in a variety of topographic settings, and future studies should include 4D aerosol impacts.

Additional efforts could also investigate the similarities and differences between naturally splitting storms over homogeneous rural terrains (Markowski and Richardson 2010) and these urban bifurcating storms. As urban building bifurcating mechanisms are always present, it is important to understand how and when they may amplify the processes acting on naturally splitting storms to produce the apparent higher observed frequency of the phenomena over urban areas. This study is thus only a first step toward a fuller understanding of urban impacts on bifurcating storms; its data are available at IUM for use by other research groups.

Acknowledgments. This work was supported by National Natural Science Foundation of China (Grants 41775078, 41605012, and 41705088), the National Key R&D Program

of China (2019YFA0607202), the Young Beijing Scholars Program (Grant 2018-007), Beijing Municipal Science and Technology Commission (Grant Z151100002115045), and the Ministry of Science and Technology of China (Grant 2015DFA20870). Thanks are given to Tim Oke for his insightful questioning of how urban areas can affect storms upwind of their boundaries and how buildings can impact storms far above their rooftops.

REFERENCES

An, N., J. Dou, J. Gonzalez, R. Bornstein, S. Miao, and L. Lin, 2020: An observational case study of synergies between an intense heat wave and the urban heat island in Beijing. *J. Appl. Meteor. Climatol.*, **59**, 605–620, https://doi.org/10.1175/JAMC-D-19-0125.1.

Ayotte, K., J. J. Finnigan, and M. R. Raupach, 1999: A second-order closure for neutrally stratified vegetative canopy flows. *Bound.-Layer Meteor.*, **90**, 189–216, https://doi.org/10.1023/A:1001722609229.

Bailey, W. G., T. R. Oke, and W. R. Rouse, 1997: *The Surface Climates of Canada*. McGill-Queen's Press, 400 pp.

Beijing Municipal Bureau of Statistics, 2016: Report on number of buildings in Beijing. BMBS, accessed 27 November 2019, http://hgk.tjj.beijing.gov.cn/ww/MenuItemAction!queryMenu.

Bornstein, R. D., 1968: Observations of the urban heat island effect in New York City. *J. Appl. Meteor.*, **7**, 575–582, https://doi.org/10.1175/1520-0450(1968)007<0575:OOTUHI>2.0.CO;2.

——, 2011: Establishment of meso-met modeling case studies to evaluate the relative roles of urban dynamics and aerosols on summer thunderstorms. *18th Conf. on Planned and Inadvertent Weather Modification*, Seattle, WA, Amer. Meteor. Soc., J5.2, https://ams.confex.com/ams/91Annual/recordingredirect.cgi/id/17137.

——, and D. S. Johnson, 1977: Urban-rural wind velocity differences. *Atmos. Environ.*, **11**, 597–604, https://doi.org/10.1016/0004-6981(77)90112-3.

——, and G. LeRoy, 1990: Urban barrier effects on convective and frontal thunderstorms. Preprints, *Fourth Conf. on Mesoscale Processes*, Boulder, CO, Amer. Meteor. Soc., 120–121.

——, and Q. Lin, 2000: Urban heat islands and summertime convective thunderstorms in Atlanta: Three case studies. *Atmos. Environ.*, **34**, 507–516, https://doi.org/10.1016/S1352-2310(99)00374-X.

——, P. Thunis, and G. Schayes, 1993: Simulation of urban barrier effects on polluted urban boundary layers using the three-dimensional URBMET/TVM model with urban topography. *Air Pollution*, Elsevier Science, 15–34.

Bougeault, P., and P. Lacarrere, 1989: Parameterization of orography-induced turbulence in a mesobeta-scale model. *Mon. Wea. Rev.*, **117**, 1872–1890, https://doi.org/10.1175/1520-0493(1989)117<1872:POOITI>2.0.CO;2.

Changnon, S. A., G. Semonin, R. T. Shealy, and R. W. Scott, 1991: Precipitation changes in fall, winter, and spring caused by St. Louis. *J. Appl. Meteor.*, **30**, 126–134, https://doi.org/10.1175/1520-0450(1991)030<0126:PCIFWA>2.0.CO;2.

Chen, F., and Coauthors, 2011: The integrated WRF/urban modeling system: Development, evaluation, and applications to urban environmental problems. *Int. J. Climatol.*, **31**, 273–288, https://doi.org/10.1002/joc.2158.

Cox, R., B. L. Bauer, and T. Smith, 1998: A mesoscale model intercomparison. *Bull. Amer. Meteor. Soc.*, **79**, 265–284, https://doi.org/10.1175/1520-0477(1998)079<0265:AMMI>2.0.CO;2.

Craig, K., and R. D. Bornstein, 2002: MM5 simulation of urban induced convective precipitation over Atlanta. Preprints, *Fourth Conf. on the Urban Environment*, Norfolk, VA, Amer. Meteor. Soc., 5–6.

Cressman, G., 1959: An operational objective analysis system. *Mon. Wea. Rev.*, **87**, 367–374, https://doi.org/10.1175/1520-0493(1959)087<0367:AOOAS>2.0.CO;2.

Dou, J., and S. Miao, 2017: Impact of mass human migration during Chinese New Year on Beijing urban heat islands. *Int. J. Climatol.*, **37**, 4199–4210, https://doi.org/10.1002/joc.5061.

——, Y. Wang, and S. Miao, 2014: Fine spatial and temporal characteristics of humidity and wind in Beijing urban area (in Chinese with English abstract). *J. Appl. Meteor. Sci.*, **25**, 559–569.

——, ——, R. Bornstein, and S. Miao, 2015: Observed spatial characteristics of Beijing urban climate impacts on summer thunderstorms. *J. Appl. Meteor. Climatol.*, **54**, 94–105, https://doi.org/10.1175/JAMC-D-13-0355.1.

Dudhia, J., 1989: Numerical study of convection observed during the winter monsoon experiment using a mesoscale two-dimensional model. *J. Atmos. Sci.*, **46**, 3077–3107, https://doi.org/10.1175/1520-0469(1989)046<3077:NSOCOD>2.0.CO;2.

Ek, M. B., K. E. Mitchell, Y. Lin, E. Rogers, P. Grunmann, V. Koren, G. Gayno, and J. D. Tarpley, 2003: Implementation of Noah land surface model advances in the National Centers for Environmental Prediction operational mesoscale Eta model. *J. Geophys. Res.*, **108**, 8851, https://doi.org/10.1029/2002JD003296.

Fan, S., M. Chen, J. Zhong, and Z. Zheng, 2009: Performance tests and evaluations of Beijing local high-resolution rapid update cycle system (in Chinese with English abstract). *Torrent. Rain Disaster*, **28**, 119–125.

——, H. Wang, M. Chen, and H. Gao, 2013: Study of the data assimilation of radar reflectivity with the WRF 3DVar (in Chinese with English abstract). *Acta Meteor. Sin.*, **71**, 527–537.

Gaffen, D., and R. D. Bornstein, 1988: Case study of urban interactions with a synoptic scale cold front. *Meteor. Atmos. Phys.*, **38**, 185–194, https://doi.org/10.1007/BF01054571.

Guo, X., D. Fu, and J. Wang, 2006: Mesoscale convective precipitation system modified by urbanization in Beijing City. *Atmos. Res.*, **82**, 112–126, https://doi.org/10.1016/j.atmosres.2005.12.007.

Haberlie, A. M., W. S. Ashley, and T. J. Pingel, 2015: The effect of urbanization on the climatology of thunderstorm initiation. *Quart. J. Roy. Meteor. Soc.*, **141**, 663–675, https://doi.org/10.1002/qj.2499.

Han, J. Y., J. J. Baik, and H. Lee, 2014: Urban impacts on precipitation. *Asia-Pac. J. Atmos. Sci.*, **50**, 17–30, https://doi.org/10.1007/s13143-014-0016-7.

He, X., Y. Li, X. Wang, L. Chen, B. Yu, and Y. Zhang, 2019: High-resolution dataset of urban canopy parameters for Beijing and its application to the integrated WRF/Urban modeling system. *J. Cleaner Prod.*, **208**, 373–383, https://doi.org/10.1016/j.jclepro.2018.10.086.

Jacobson, M., S. Nghiem, A. Sorichetta, and N. Whitney, 2015: Ring of impact from the mega-urbanization of Beijing between 2000 and 2009. *J. Geophys. Res. Atmos.*, **120**, 5740–5756, https://doi.org/10.1002/2014JD023008.

Jiang, X., Y. Luo, D. Zhang, and M. Wu, 2020: Urbanization enhanced summertime extreme hourly precipitation over the Yangtze River Delta. *J. Climate*, **33**, 5809–5826, https://doi.org/10.1175/JCLI-D-19-0884.1.

Kain, J. S., 2004: The Kain–Fritsch convective parameterization: An update. *J. Appl. Meteor.*, **43**, 170–181, https://doi.org/10.1175/1520-0450(2004)043<0170:TKCPAU>2.0.CO;2.

Krayenhoff, S., and J. Voogt, 2010: Impacts of urban albedo increase on local air temperature at daily–annual time scales: Model results and synthesis of previous work. *J. Appl. Meteor. Climatol.*, **49**, 1634–1648, https://doi.org/10.1175/2010JAMC2356.1.

Kuang, W., and G. Du, 2011: Analyzing urban population spatial distribution in Beijing proper (in Chinese with English abstract). *J. Geo-Inf. Sci.*, **13**, 506–512, https://doi.org/10.3724/SP.J.1047.2011.00506.

Kusaka, H., H. Kondo, Y. Kikegawa, and F. Kimura, 2001: A simple single-layer urban canopy model for atmospheric models: Comparison with multi-layer and slab models. *Bound.-Layer Meteor.*, **101**, 329–358, https://doi.org/10.1023/A:1019207923078.

Li, D., E. Bou-Zeid, M. L. Baeck, S. Jessup, and J. A. Smith, 2013: Modeling land surface processes and heavy rainfall in urban environments: Sensitivity to urban surface representations. *J. Hydrometeor.*, **14**, 1098–1118, https://doi.org/10.1175/JHM-D-12-0154.1.

Liang, X., and Coauthors, 2018: SURF: Understanding and predicting urban convection and haze. *Bull. Amer. Meteor. Soc.*, **99**, 1391–1413, https://doi.org/10.1175/BAMS-D-16-0178.1.

Liu, Y., W. He, and Y. Xu, 2015: Measure of Beijing urban underlying surface heterogeneity characteristic (in Chinese with English abstract). *J. Nanjing Univ. Info. Sci. Technol. Nat. Sci. Educ.*, **7**, 444–450.

Loose, T., and R. D. Bornstein, 1977: Observations of mesoscale effects on frontal movement through an urban area. *Mon. Wea. Rev.*, **105**, 563–571, https://doi.org/10.1175/1520-0493(1977)105<0563:OOMEOF>2.0.CO;2.

Lorenz, J. M., R. Kronenberg, C. Bernhofer, and D. Niyogi, 2019: Urban rainfall modification: Observational climatology over Berlin, Germany. *J. Geophys. Res Atmos.*, **124**, 731–746, https://doi.org/10.1029/2018JD028858.

Luo, Y., M. Wu, F. Ren, J. Li, and W.-K. Wong, 2016: Synoptic situations of extreme hourly precipitation over China. *J. Climate*, **29**, 8703–8719, https://doi.org/10.1175/JCLI-D-16-0057.1.

Markowski, P., and Y. Richardson, 2010: *Mesoscale Meteorology in Midlatitudes*. Wiley-Blackwell, 407 pp.

Martilli, A., A. Clappier, and M. W. Rotach, 2002: An urban surface exchange parameterization for mesoscale models. *Bound.-Layer Meteor.*, **104**, 261–304, https://doi.org/10.1023/A:1016099921195.

Miao, S., F. Chen, Q. Li, and S. Fan, 2011: Impacts of urban processes and urbanization on summer precipitation: A case study of heavy rainfall in Beijing on 1 August 2006. *J. Appl. Meteor. Climatol.*, **50**, 806–825, https://doi.org/10.1175/2010JAMC2513.1.

——, J. Dou, F. Chen, J. Li, and A. Li, 2012: Analysis of observations on the urban surface energy balance in Beijing. *Sci. China Earth Sci.*, **55**, 1881–1890, https://doi.org/10.1007/s11430-012-4411-6.

Mitra, C., and J. M. Shepherd, 2016: Urban precipitation: A global perspective. *The Routledge Handbook of Urbanization and Global Environmental Change*, K. C. Seto, W. D. Solecki, and C. A. Griffith, Eds., Routledge, 152–168.

Mlawer, E. J., S. J. Taubman, P. D. Brown, M. J. Iacono, and S. A. Clough, 1997: Radiative transfer for inhomogeneous atmospheres: RRTM, a validated correlated-*k* model for the longwave. *J. Geophys. Res.*, **102**, 16 663–16 682, https://doi.org/10.1029/97JD00237.

Niyogi, D. T., P. Pyle, M. Lei, S. P. Arya, C. M. Kishtawal, M. Shepherd, F. Chen, and B. Wolfe, 2011: Urban modification of thunderstorms: An observational storm climatology and model case study for the Indianapolis urban region. *J. Appl. Meteor. Climatol.*, **50**, 1129–1144, https://doi.org/10.1175/2010JAMC1836.1.

Oke, T. R., 1987: *Boundary Layer Climates*. 2nd ed. Routledge, 435 pp.

——, 1988: The urban energy balance. *Prog. Phys. Geogr.*, **12**, 471–508, https://doi.org/10.1177/030913338801200401.

——, G. Mills, A. Christen, and J. A. Voogt, 2017: *Urban Climates*. Cambridge University Press, 527 pp.

Pielke, R. A., Sr., 2013: *Mesoscale Meteorological Modeling*. 3rd ed. Academic Press, 276 pp.

Salamanca, F., A. Krpo, A. Martilli, and A. Clappier, 2010: A new building energy model coupled with an urban canopy parameterization for urban climate simulations—Part I. Formulation, verification, and sensitivity analysis of the model. *Theor. Appl. Climatol.*, **99**, 331–344, https://doi.org/10.1007/s00704-009-0142-9.

Schlunzen, K. H., and J. J. Katzfey, 2003: Relevance of subgrid-scale land-use effects for mesoscale models. *Tellus*, **55A**, 232–246, https://doi.org/10.1034/j.1600-0870.2003.00017.x.

Schlünzen, K. H., P. Hoffmann, G. Rosenhagen, and W. Riecke, 2010: Long-term changes and regional differences in temperature and precipitation in the metropolitan area of Hamburg. *Int. J. Climatol.*, **30**, 1121–1136, https://doi.org/10.1002/joc.1968.

Shem, W., and J. M. Shepherd, 2009: On the impact of urbanization on summertime thunderstorms in Atlanta: Two numerical model case studies. *Atmos. Res.*, **92**, 172–189, https://doi.org/10.1016/j.atmosres.2008.09.013.

Shepherd, J. M., 2013: Impacts of urbanization on precipitation and storms: Physical insights and vulnerabilities. *Climate Vulnerability: Understanding and Addressing Threats to Essential Resources*, Academic Press, 109–125.

——, H. Pierce, and A. J. Negri, 2002: Rainfall modification by major urban areas: Observations from space borne rain radar on the TRMM satellite. *J. Appl. Meteor.*, **41**, 689–701, https://doi.org/10.1175/1520-0450(2002)041<0689:RMBMUA>2.0.CO;2.

Sun, J., H. Wang, L. Wang, F. Liang, Y. Kang, and X. Jiang, 2006: The role of urban boundary layer in local convective torrential rain happening in Beijing on 10 July 2004 (in Chinese with English abstract). *Chin. J. Atmos. Sci.*, **30**, 221–234.

——, ——, L. Lei, B. Yu, and Q. Ding, 2015: The fundamental feature of the extreme severe rain events in the recent 10 years in the Beijing area. *Acta Meteor. Sin.*, **73**, 609–623.

Thompson, G., R. Rasmussen, and K. Manning, 2004: Explicit forecasts of winter precipitation using an improved bulk microphysics scheme. Part I: Description and sensitivity analysis. *Mon. Wea. Rev.*, **132**, 519–542, https://doi.org/10.1175/1520-0493(2004)132<0519:EFOWPU>2.0.CO;2.

Wang, X., X. Li, and Z. Feng, 2010: Research on urban extension based on Shannon entropy (in Chinese with English abstract). *China Popul. Resour. Environ.*, **20**, 88–92.

Wilson, N. B., and R. H. Shaw, 1977: A higher order closure model for canopy flow. *J. Appl. Meteor.*, **16**, 1197–1205, https://doi.org/10.1175/1520-0450(1977)016<1197:AHOCMF>2.0.CO;2.

Wu, M., Y. Luo, F. Chen, and W. K. Wong, 2019: Observed link of extreme hourly precipitation changes to urbanization over coastal south China. *J. Appl. Meteor. Climatol.*, **58**, 1799–1819, https://doi.org/10.1175/JAMC-D-18-0284.1.

Wu, X., X. Wang, X. Zeng, and L. Xu, 2000: The effect of urbanization on short duration precipitation in Beijing (in Chinese with English abstract). *J. Nanjing Inst. Meteor.*, **23**, 68–72.

Yu, M., and Y. Liu, 2015: The possible impact of urbanization on a heavy rainfall event in Beijing. *J. Geophys. Res. Atmos.*, **120**, 8132–8143, https://doi.org/10.1002/2015JD023336.

Zhang, D.-L., 2020: Rapid urbanization and more extreme rainfall events. *Sci. Bull.*, **65**, 516–518, https://doi.org/10.1016/j.scib.2020.02.002.

——, M. S. Jin, Y. Shou, and C. Dong, 2019: The influences of urban building complexes on the ambient flows over the Washington–Reston region. *J. Appl. Meteor. Climatol.*, **58**, 1325–1336, https://doi.org/10.1175/JAMC-D-19-0037.1.

Zhang, Y., S. Miao, Y. Dai, and R. Bornstein, 2017: Numerical simulation of urban land surface effects on summer convective rainfall under different UHI intensity in Beijing. *J. Geophys. Res. Atmos.*, **122**, 7851–7868, https://doi.org/10.1002/2017JD026614.

Zhong, S., and X. Yang, 2015: Ensemble simulations of the urban effect on a summer rainfall event in the Great Beijing Metropolitan Area. *Atmos. Res.*, **153**, 318–334, https://doi.org/10.1016/j.atmosres.2014.09.005.